Multi-Frequency Satellite Approaches for Snow on Sea Ice

Polar+ Snow on Sea Ice (PSSI)

Deliverable 1:

Requirement Baseline Document (RB)

Document History

Version	Date	Updated by	Reason
1.0	*12/07/21*	*M.Tsamados*	*Initial draft in preparation to PM1*
2.0	*30/08/21*	*Completion by PSSI partners Isobel Lawrence and S. Hendricks*	*Edits to initial draft*
2.1	*17/09/21*	*Review and correction by M. Tsamados*	*Finalize version*

Detailed History of Changes

Version	Section	Updated by	Details

Contact details: Dr. Michel Tsamados
UCL, Earth Sciences
5 Gower Place
London WC1E 6BS
email m.tsamados@ucl.ac.uk

The project website is http://www.cpom.ucl.ac.uk/snow-on-sea-ice/index.html

printed on 18/01/2022

Copyright © 2021 University College London. All rights reserved. Reproduction of the whole or any part of this document without permission is prohibited.

Table of Contents

Acronyms and Abbreviation

AltiKa – Ka-band Altimeter
AMSR-E - Advanced Microwave Scanning Radiometer - Earth Observing System
ATBD – Algorithm Theoretical Basis Document
AVHRR - Extended Advanced Very High Resolution Radiometer
AWI – Alfred Wegener Institute
CICE – The Los Alamos Sea Ice Model
CRREL - Cold Regions Research and Engineering Laboratory
CryoVEx - CryoSat Validation Experiment
CS2 – CryoSat-2
DuST – Dual-altimeter Snow Thickness
ECMWF – European Centre for Medium-range Weather Forecasts
Envisat – Environmental Satellite
EO – Earth Observation
ERS – European Remote Sensing Satellite
ESA – European Space Agency
EXPRO – Express Procurement
FBEM - Facet-Based numerical Echo Model
FMI – Finnish Meteorological Institute
FYI – First-Year Ice
GLAS – Geoscience Laser Altimeter System
IABP – International Arctic Buoy Program
IAR – Impact Assessment Report
ICESat – Ice, Cloud and land Elevation Satellite
IMB – Ice Mass-balance Buoy
ITT – Invitation To Tender
KO – Kick-Off
KuKa – Ku (radar) / Ka (radar) snow thickness product
KuLa – Ku (radar) / Laser snow thickness product
LEGOS - Laboratoire d'Etudes en Géophysique et Océanographie Spatiales
LIM – Louvain-la-Neuve Sea Ice Model
MAF – Management, Administrative and Financial proposal
MYI – Multi-Year Ice
NASA – National Aeronautics and Space Administration
NCEP – National Centers for Environmental Prediction
NSIDC – National Snow and Ice Data Centre
OIB - Operation IceBridge
PP – Project Partner
RA2 – Radar Altimeter 2
RB – Requirement Baseline
SAR – Synthetic Aperture Radar
SARAL – Satellite for Argos and AltiKa
SHEBA - Surface Heat Budget of the Arctic Ocean
SIPN – Sea Ice Prediction Network
SMOS - Soil Moisture and Ocean Salinity satellite
SnoDSI – SNOw on Drifting Sea Ice
SOW – Statement Of Work
SR – Scientific Roadmap
SSM/I - Special Sensor Microwave Imager
SSMIS – SSM/I Sounder
STSE – Support To Science Element
SWE – Snow Water Equivalent
TP – Technical Proposal
UiT – Arctic University of Norway
UCL – University College London
W99 – Warren et al. (1999) snow climatology
WP – Work Package
YOPP – Year of Polar Prediction

1. PURPOSE AND SCOPE

1.1. Project objectives

The primary objective of this project is to investigate multi-frequency approaches to retrieve snow thickness over all types of sea ice surfaces in the Arctic and provide a state-of-the-art snow product.

Our approach follows ESA ITT recommendations to prioritise satellite-based products and will benefit from the recent 'golden era in polar altimetry' with the successful launch of the laser altimeter ICESat-2 in 2018 complementing data provided by the rich fleet of radar altimeters, CryoSat-2, Sentinel-3 A/B, AltiKa. Our primary objective is to produce an optimal snow product over the recent 'operational' period.

This will be complemented by additional snow products covering a longer periods of climate relevance and making use of historical altimeters (Envisat, ICESat-1) and passive microwave radiometers for comparison purposes (SMOS, AMSRE, AMSR-2). In addition to snow thickness, and as a secondary objective, we will explore other snow characteristics (snow density, snow metamorphism, scattering horizon, roughness, etc) and compare these results with in-situ, airborne and other snow on sea ice products including from model studies and reanalysis on drifting sea ice products.

In preparation for future multi-frequency missions, we will put an emphasis on uncertainty analysis of our snow product, the impact of the snow on the sea ice thickness retrieval, and on climate physics via model runs with snow initialisation and data assimilation. Finally, learning from past and present campaigns (i.e. CryoVex, MOSAiC) we will propose methodologies for effective future snow and sea ice thickness airborne validation campaigns via innovative inverse modelling approaches and airborne retrackers.

The work for the Polar+ Snow (Theme 1) project is organized in a linear structure of Work Packages (WPs) as shown in Figure 1. The contents of the work packages are described in detail below.

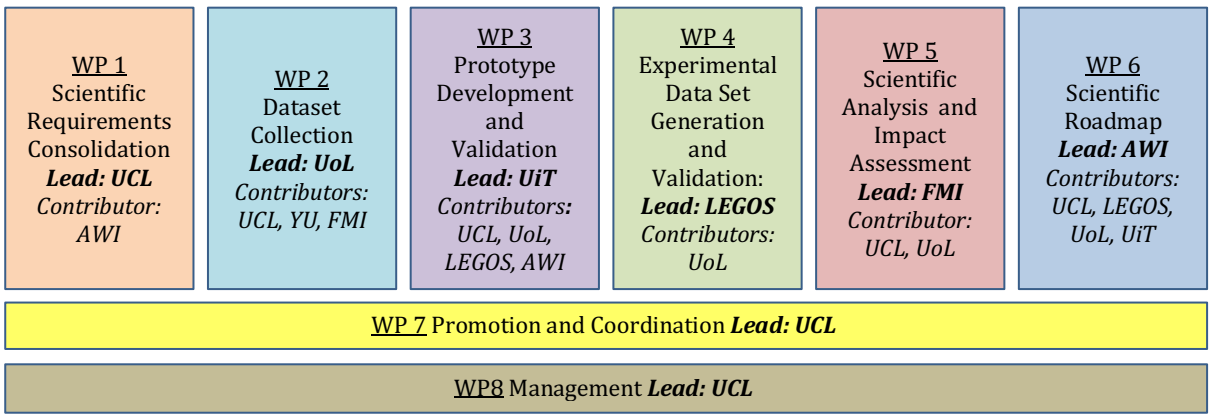

Figure 1 – Proposed Work Package Structure.

The aims of Polar+ will be achieved through the work contained within eight work packages (WP1 to

WP8).

- WP1 and WP2 involve the preparatory work ahead of generating the methods; specifically, they are concerned with assessing the scientific challenges posed by the Polar+ Theme 1, reviewing the potential data sets, methods and study regions, and collecting all of the necessary data, respectively.
- WP3 involves developing the algorithms and prototype Multi-Frequency snow thickness and error analysis for our two main streams of radar-radar and radar-laser products.
- WP4 is concerned with implementation and demonstration of the experimental gridded datasets generation and their validation against a suite of in-situ (i.e. MOSAiC) and airborne measurements (i.e. CryoVex, OIB).
- WP5 will be assessing the potential impact of the products both in terms of sea ice thickness retrievals and model improvements.
- WP6 is concerned with drawing out the Scientific Roadmap, which will outline potential avenues for future research and operational activities.
- WP7 consists of the promotion and coordination of the project.
- WP8 entails the management of the project. These work packages address and mirror the tasks outlined in the SOW.

Specific project tasks are detailed in the Work Package description sheets (Appendix B; Management, Administrative and Financial Proposal, Ref: ESA/ AO/1-10061/19/I-EF – 'EXPRO – Polar+'). The project will focus on developing a state-of-the-art multi-frequency and multi-sensor snow depth. The task proposed by ESA are summarized below following the ESA proposal template.

1.2. Document objectives

This document is our study's Deliverable 1, the Requirement Baseline (RB) Document. It summarizes the results of WP1 of the study, the Scientific Requirements Consolidation. It consolidates the preliminary scientific requirements for snow on sea ice observations and applications. The task is broken down into the following sub-tasks

- T1.1: Purpose and scope of the project
- T1.2: Role of snow in the Arctic climate system
- T1.3: Role of snow for sea ice thickness retrievals
- T1.4: Knowledge gaps and uncertainty of snow on sea ice
- T1.5: Identification of key areas for test and validation
- T1.6: Survey of existing snow on sea ice datasets
- T1.7: Informing present and future snow on sea ice initiatives

2. ROLE OF SNOW IN THE ARCTIC CLIMATE SYSTEM

2.1. Summary of inputs, tasks and outputs

Inputs required to Start:
• SoW [EOP-SDR/SOW/087-17/DFP]
• Proposal [UCL-PRO-19-MT1]
Task Description:
• Review major scientific questions related to the polar climate that snow on sea ice can help address
• Describe current understanding of seasonal snow evolution
• Review impact of snow on sea ice volume and ocean
Outputs:
• Contribution D1: Requirement Baseline (RB)

2.2. Seasonal evolution of snow

The climate of the Arctic is changing rapidly with well documented repercussions on the sea ice extent, thickness, speed and ice age among other characteristics (Stroeve & Notz, 2018). Changes in the snow cover remain harder to monitor with limited in-situ and airborne observations (Shalina et al, 2020) covering only parts of the Arctic basin and biased towards the spring season (see WP2). Webster et al (2014), compared over the central Arctic and Canadian archipelago the Warren climatology (Warren et al., 1999) of the 1950s-1990s to an updated climatology over the Operation IceBridge (OIB) period 2009-2013 and found a decline in snow depth of 37% and 50% over first year ice (FYI) and multi-year ice (MYI) respectively. This decline contrasts with very deep snow measured in the Atlantic sector during the N-ICE2015 campaign (Merkouriadi et al, 2017) while new in-situ snow measurements are currently being collected as part of the MOSAiC expedition.

Every year, snow accumulates on the surface of the sea ice from the end of the summer season (September) and the snow depth grows steadily until the end of winter when it stabilizes at roughly 20-30 cm up until the beginning of the melt season (May) (Figure 2). At that time, the melt of the entire snow layer happens suddenly over a period of less than 2 weeks leading to the formation of melt ponds and resulting in a significant decrease of the albedo at the surface of the ice throughout the summer season.

In the same manner that sea ice insulates the Arctic Ocean from the overlying atmosphere, the snow, that generally has a higher albedo than ice (with values ranging from 0.8 to 0.9 for clean snow (Wiscombe and Warren, 1980)), plays a leading role in the surface energy balance. During the annual freeze-up period, snow acts as an insulator between the sea ice and the cold atmosphere, retarding ice growth (Sturm et al, 2002). In the melt season, snow presents a higher albedo than ice and has its own latent heat of fusion to overcome before melting of ice is initiated from the surface. Modelling studies (Rae et al, 2014) have shown that in the Arctic, the sea ice thickness is most sensitive to the albedo of the overlying snow layer (because of its influence on surface melt) and the thermal conductivities of ice and snow (because of their role in regulating heat flux from the ocean to the atmosphere through the ice).

In addition to the average seasonal cycle (Figure 2), the snow pack on Arctic sea ice exhibits large spatial and temporal variability. Because of the thin, dynamic, and brittle nature of the sea ice, which can fracture and form ridges or leads, the snow cover is strongly coupled to fundamental sea ice characteristics (i.e., concentration, deformation, etc.). The result is that the physics of snow on sea ice differs significantly from the physics of terrestrial snow covers. The complex interactions between snow and sea ice are also strongly influenced by the ocean and the atmosphere.

In fact, while snow accumulation is primarily driven by precipitation, its deposition is largely controlled by the winds and the nature of the sea ice on which it falls (Strum and Massom, 2009). Over seasonal sea ice a significant fraction of the snow is blown away and lost to the open water in contrast to MYI, where snow accumulation is larger. This wind-driven redistribution of snow from sea ice to open water is more effective over relatively un-deformed level ice, unlike over deformed ice where snow tends to accumulate in the lee of pressure ridges. As a result, the snow thickness is spatially heterogeneous and varies more or less rapidly depending on the type of sea ice (Figure 3). Snow lost to the ocean either by wind redistribution or summer-melt is also an important component of the Arctic Ocean fresh water budget (Warren et al., 1999).

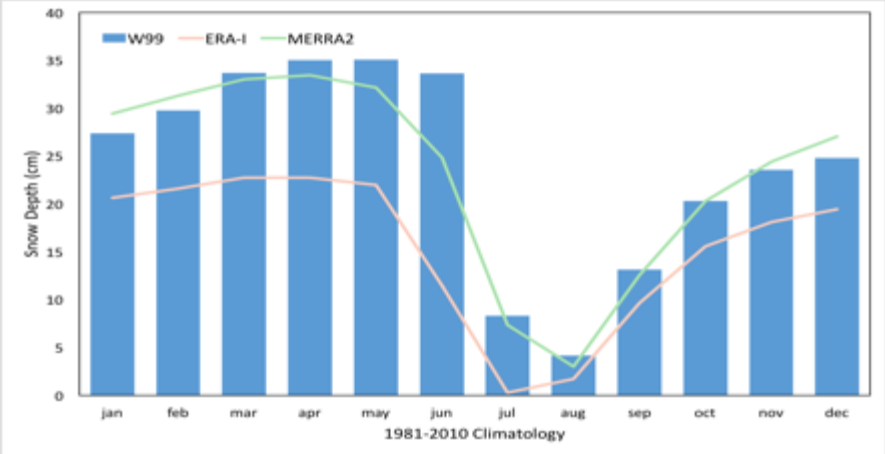

Figure 2 - Seasonal pan-Arctic snow thickness evolution for the Warren climatology (Warren et al, 1999) and the SNOWMODEL (Stroeve et al., personal communication) forced with two different reanalysis products.

Modelling studies suggest that snow processes can have complex interactions with sea ice, the ocean and atmosphere (Blazey et al., 2013; Lecomte et al., 2014) and may influence Arctic predictability (Blanchard-Wrigglesworth, 2014). Utilizing the knowledge derived from a new snow on sea ice product, in combination with a variety of remotely sensed data and reanalyses, we wish to better understand the trade-offs between precipitation/snow accumulation and the seasonal energetics of melt, particularly for 'big' melt years such as 2007 and 2012.

2.3. Impact on climate: sea ice volume and ocean

As was the case in Arctic+ Snow we will examine the consequences of using different snow thickness products on the simulation of sea ice thickness and freshwater in two numerical sea ice models: the coupled sea ice ocean configurations NEMO-LIM3 (Uotila et al., 2017) and NEMO-CICE (Schroeder et al., 2019). Figure 3 shows snow thickness difference maps that were computed between the NEMO-

LIM3 own snow thickness parameterization, and the DuST snow thickness product. It can be seen that differences are mostly negative, i.e. the model's snow thickness is much smaller than that of the DuST product. We will use the same PPs as in Arctic+ Snow project to drive this activity but instead of DuST, we will assimilate our two new multi-frequency products (KuKa-Snow and KuLa-Snow) into the latest versions on the models that are being continuously developed at FMI and CPOM.

The impacts on model simulations and potential freshwater fluxes to the North Atlantic are best summarized by time series of Arctic ice volume (Figure 43 in the Proposal [UCL-PRO-19-MT1]). Using different snow products for model initialization and updates, differences of up to 1500 km^3 result after initialization in Feb/March. This is approximately 5 % of the maximum Arctic ice volume of 30,000 km^3. The positive differences mean that the model's original ice thickness is much larger than when the new products are used, i.e. the NEMO-LIM standard run produces more ice due to its thinner snow cover. Note that the differences are largest for the snow on drifting sea ice product (SnoDSI) that will not be further developed as part of this project. Instead, we will explore the impact on the total volume of ice from assimilating the multi-frequency products (KuKa & KuLa) developed in WP3 and WP4.

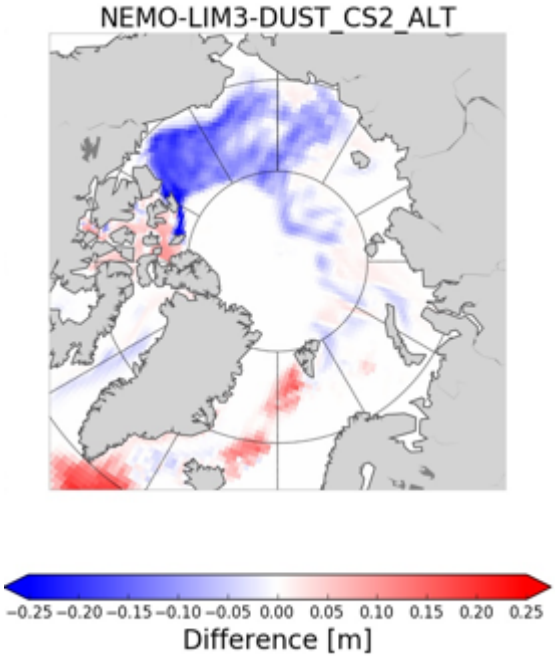

Figure 3 - Snow thickness differences between NEMO-LIM3 standard runs and runs which used the DuST snow thickness product. Results for Feb/Mar 2015

Another important application of the snow product will be to assess in sea ice – ocean coupled model runs the role that snow plays on the ocean. In particular we will be looking at the new snow product's impact on under-ice light field and primary productivity. We will also be assessing the impact of the snow product on the freshwater fluxes into Arctic Ocean and North Atlantic and its impact on the thermohaline circulation. We note that the differences in sea ice volume of the order of 100s km^3 seen in the model simulation are comparable to the yearly volume of freshwater additional melt water released to the ocean from the melting glaciers and ice caps in the Arctic and are therefore likely to significantly modify the ocean circulation and stratification in the models.

3. ROLE OF SNOW IN SEA ICE THICKNESS RETRIEVALS

3.1. Summary of inputs, tasks and outputs

Inputs required to Start:
• SoW [EOP-SDR/SOW/087-17/DFP]
• Proposal [UCL-PRO-19-MT1]
Task Description:
• Review of altimetry sea ice thickness processing retrievals
• Review propagation of uncertainty of snow to ice thickness
• Review impact assessment of new snow on sea ice products
Outputs:
• Contribution D1: Requirement Baseline (RB)

3.2. Snow for satellite sea ice thickness retrievals

In order to understand the observed changes in sea ice thickness we first need to come to terms with exactly what those changes have been. The majority of remotely sensed ice thickness data, whether derived from laser or radar altimetry, is heavily influenced by snow accumulation upon ice (Figure 4). Hence there is a distinct need to understand the depth, density and distribution and impact of snow on sea ice. The shift in the Arctic sea ice regime toward a predominantly seasonal ice pack also means that climatological snow information collected prior to the 1990s (e.g. Warren et al., (1999)) may not be as pertinent as it once was. Without sufficient knowledge of the snow cover, we cannot address important scientific questions, such as how significantly is sea ice mass declining, as accurately as is necessary.

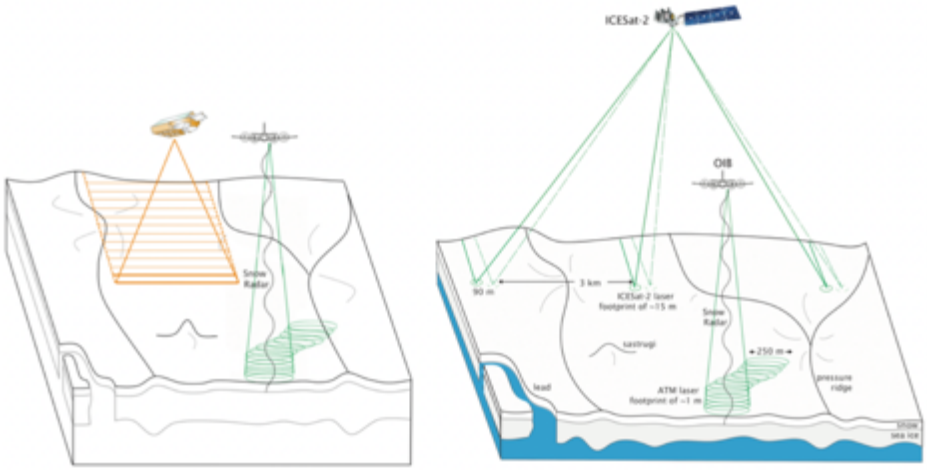

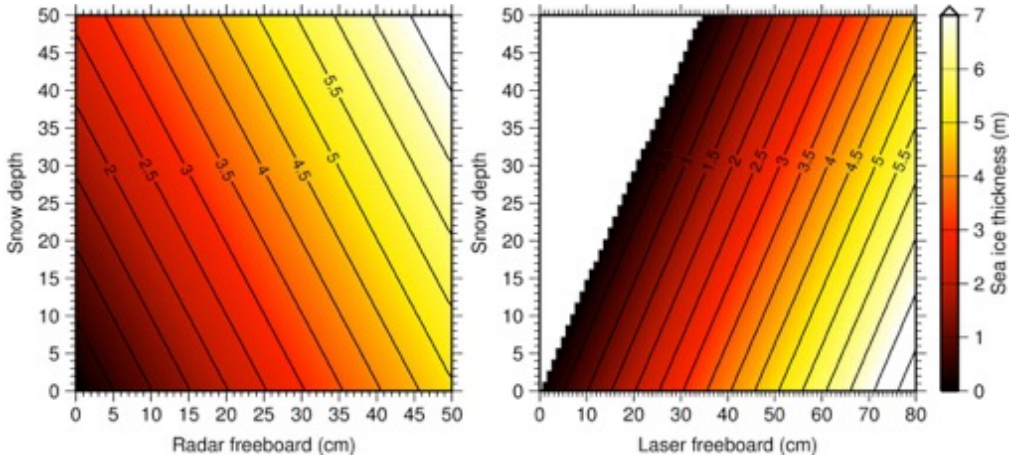

Figure 4: Schematics of the radar altimeter CryoSat-2 (top left) and laser altimeter ICESat-2 (top right). The sea ice thickness for varying radar (bottom-left) and laser (bottom-right) freeboard and snow depth.

To illustrate the importance of snow depth for linking radar and laser altimeter-derived sea ice thickness, consider a sea ice floe with sea ice freeboard of 15cm and a snow layer depth of 20cm (Figure 4). For typical densities of sea ice, the ocean surface and snow of 920kgm^{-3}, 1024kgm^{-3} and 320kgm^{-3}, the sea ice thickness is 2.1m. However, if the snow layer depth is unknown and is taken to be a climatological value of, say, 30cm, the resulting thickness calculated from a laser altimeter will be 1.4m, and the thickness from a radar altimeter will be 2.6m.

3.3. Propagating snow uncertainty to sea ice thickness

Figure 5 summarizes the main sources of bias in sea ice thickness retrievals from radar altimetry and shows that in addition to snow thickness biases other important contribution come into play when interpreting the altimetry signals. The snow and ice density play a leading order as can be seen in the hydrostatic equation relating sea ice thickness, H_I, to snow thickness, H_S, and radar freeboard, F_R :

$$H_I = \frac{\rho_s}{\rho_w - \rho_i} H_S + \frac{\rho_w}{\rho_w - \rho_i} F_R \,.$$

Another dominant contributor to sea ice uncertainty comes from the sea ice and snow surface roughness within the footprint of the radar (and laser) altimeter that can modify the perceived scattering horizon within the snow pack (Landy et al, 2019). Finally, the vertical structure within the snow pack and its interactions with the incoming electro-magnitude waves significantly modulate the penetration depth and volume scattering of the radar echoes and was shown to be a large source of biases in current retrieval methodologies (Willatt et al, 2011).

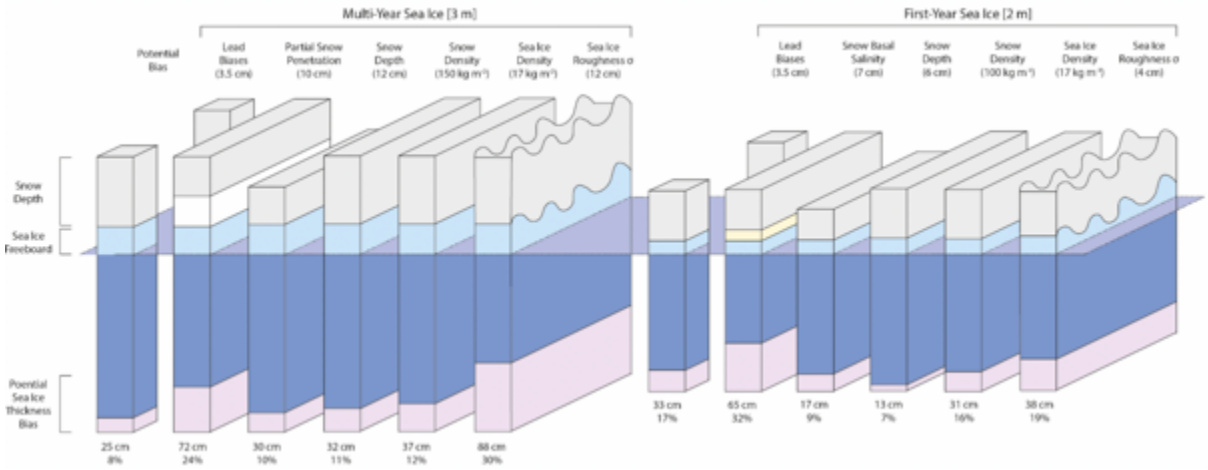

Figure 5 – Schematic diagram of the potential systematic bias in CryoSat-2-derived sea ice thickness introduced from each principal source of uncertainty: penetration and volume scattering over multi-year ice, lead biases, snow depth, snow density, basal salinity from wicking over first-year ice, sea ice density, and sea ice surface roughness (Landy et al, in review).

Apart from the importance of the snow for altimetric ice thickness retrievals, snow thickness and metamorphosis also affect microwave emissivity and therefore the brightness temperatures measured by satellite passive microwave radiometers. For example, combining a thermodynamic snow model forced by ERA interim data and a microwave emission model for layered snowpacks, Willmes et al. (2014) showed that snow metamorphosis can cause emissivity variations which correspond to differences of >10% in passive microwave ice concentration algorithms.

Therefore, an important step towards improving the accuracy of the satellite-derived sea ice thickness (and concentration) is having better estimates of snow thickness and density and their respective inter-annual variability. This is the primary goal of the novel snow thickness and density products that we will set out in this proposal. Secondly, these products will be used for process studies of seasonal and inter-annual-scale variability of snow depth. Finally, they will be used to be validate snow on sea ice from coupled global models that currently provide seasonal forecasts and projections of sea ice extent and thickness through the 21st century.

A primary expectation of the project is to reduce the random and systematic components of the sea ice thickness uncertainty budget. Presently the random uncertainty on the gridded sea ice thickness products from CryoSat-2 is around 25% of total thickness (Tilling et al., 2017) and the systematic uncertainty can be up to 30% from any single component of bias (Landy et al., In Review). We find that snow depth uncertainty dominates in fall and ice density uncertainty impact scales directly with freeboard/thickness and becomes the most important factor in April (Figure 6). By combining observations from multiple missions and by testing snow depth and freeboard products from our team's diverse set of processing chains, we anticipate significant reductions in some of the primary ice thickness uncertainties, including predictably the snow depth uncertainty, but also uncertainties in Ku/Ka-band radar penetration factors and from the impact of surface roughness within different mission footprints on retracked snow and ice freeboards. Using optimal interpolation techniques to resample raw datasets to final product grids will enable robust determination of inter-mission uncertainties and their covariances (Lawrence et al., 2018; Pujol et al., 2016).

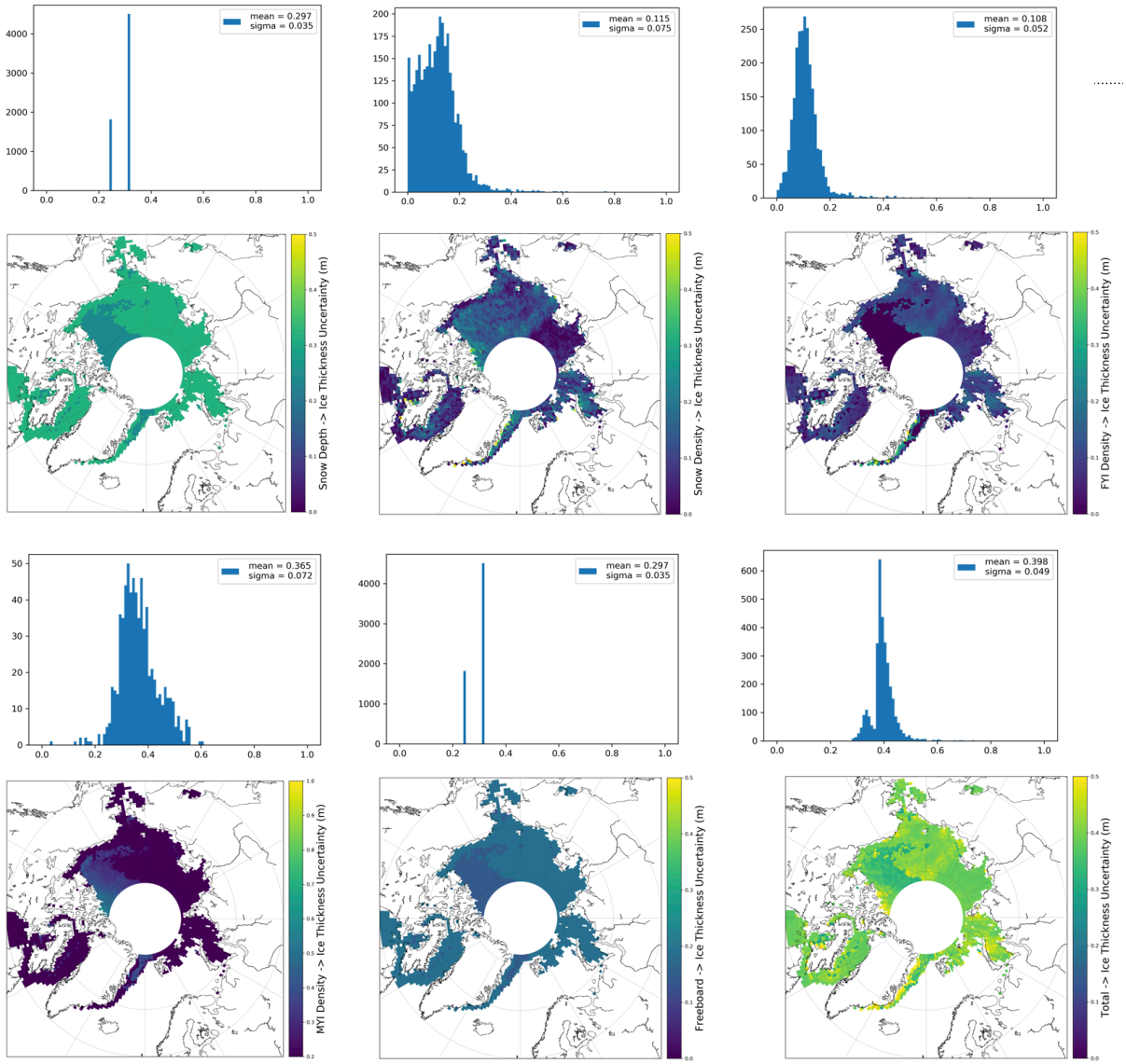

Figure 6 – Contributions to sea ice thickness uncertainties for April 2016. Credit: Michel Tsamados.

3.4. Integration of snow product for sea ice thickness retrievals

After product generation and validation we will study the impact of our snow products on satellite altimetry ice thickness retrievals. Results obtained as part of ESA's Arctic+ Snow project showed that differences in snow thickness have a leading order effect on radar retrieval of sea ice thickness. The general underestimation of snow thickness by DuST lead to an underestimation of ice thickness by as much as 0.8 m. As the thickness of snow on sea ice remains largely unknown and as the representativeness and long-term variability of the Warren climatology are unclear, these examples also give an idea of the ranges of uncertainties caused by unknown snow thickness.

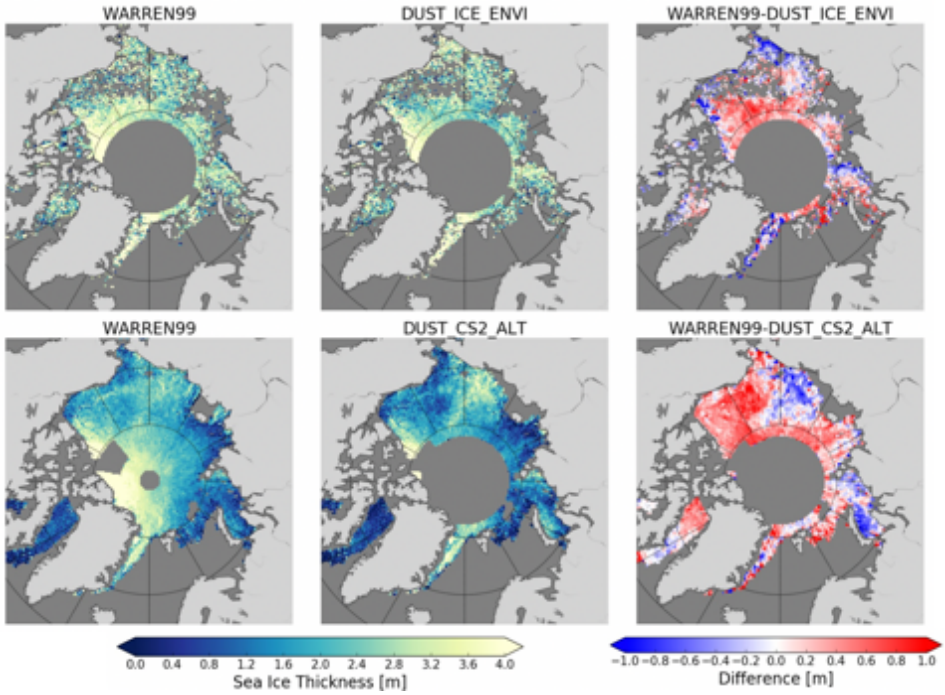

Figure 7 - Typical CryoSat ice thickness maps retrieved with the DuST snow thickness products. Left: reference ice thickness using the Warren et al. (1999) snow thickness climatology. Center: ice thickness map using DuST snow thickness products. Right: Difference between ice thickness using Warren et al. (1999) and DuST. Top row: March 2005 for DuST (Envisat/ICESat-1). Bottom row: April 2014 for DuST (CryoSat-2/AltiKa).

Figure 7 shows the impact of the DuST (Envisat/ICESat-1) and DuST (CryoSat-2/AltiKa) on the sea ice thickness retrievals when assimilated into the PySIRAL (AWI/FMI) processing chain. These will inform our project as they are the analogous of our KuLa and KuKa snow products developed in WP3 and WP4. FMI will coordinate this WP (as was the case during Arctic+ Snow) and integrate the new snow products into PySIRAL, but we expect all PPs to assimilate the new snow products in their sea ice processing chains. For example, recent analysis of the role of the snow cover into the UiT and UCL processing chains (Figure 6; Landy et al, in review) showed that systematic uncertainties relating to snow properties are estimated as 10-25% of total thickness. Thus, improving the accuracy and reliability of a pan-Arctic snow depth product demonstrates a clear avenue for drastically improving ice thickness products.

Our new snow products will also be integrated in the IS2 processing chains in development within our PP groups and at NASA. Figure 8 illustrates some recent results that incorporate the NASA Eulerian Snow on Sea Ice Model (NESOSIM) within the NASA Goddard IS2 sea ice thickness processing chain compared to CS2 thicknesses derived with the modified Warren climatology (Tilling et al, 2018).

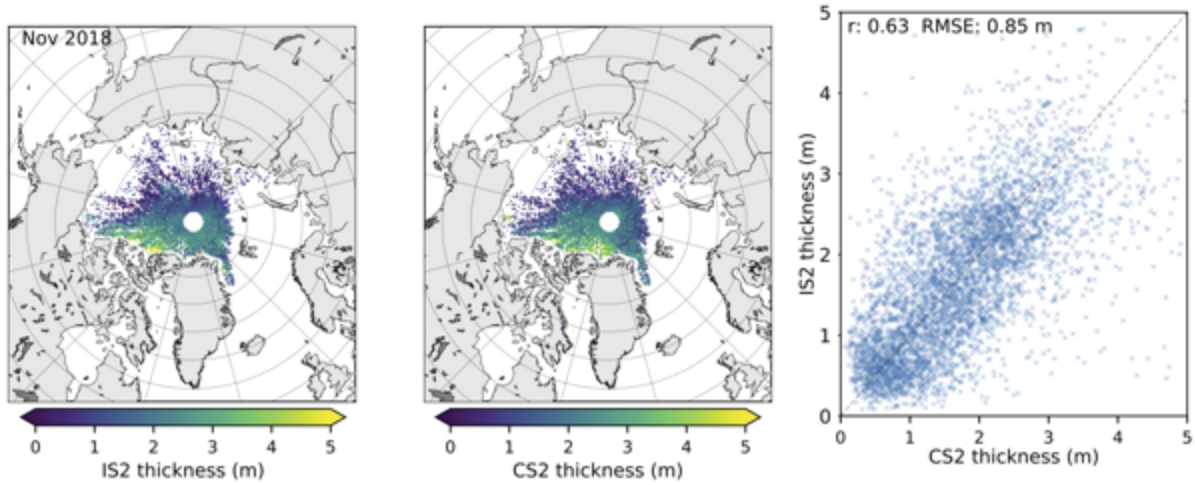

Figure 8 – Preliminary comparison of sea ice thickness derived from ICESat-2 (ATL10) and CryoSat-2 freeboards using NESOSIM snow depth and density) for data collected in November 2018. More work needs to be done to explore these comparisons across the available CryoSat-2 products and using different input assumptions. Credit: NASA PP Alek Petty.

4. SNOW ON SEA ICE UNCERTAINTY AND KNOWLEDGE GAPS

4.1. Summary of inputs, tasks and outputs

Inputs required to Start:
• SoW [EOP-SDR/SOW/087-17/DFP]
• Proposal [UCL-PRO-19-MT1]
Task Description:
• Review main snow on sea ice uncertainties
• Identify key gaps in radar freeboard retrievals
• Identify key gaps in snow retrievals
• Identify key gaps in laser freeboard retrievals
Outputs:
• Contribution D1: Requirement Baseline (RB)

4.2. Main source of snow characteristics uncertainty

The geophysical properties of snow accumulated on sea ice vary significantly over short spatial and temporal scales. Snow is deposited on the ice in discrete storm events, is redistributed across the ice surface by winds, and accumulates on the windward side of pressure ridges or in snowdrifts on level ice (Sturm et al., 2002). A number of snow geophysical properties relevant for microwave remote sensing, including the snow grain size, density, brine content, wetness and layering (Langlois and Barber, 2007), as well as the snow depth, can therefore be heterogenous over snow drift scales (10s meters) and time periods of days-weeks (Sturm et al., 2002). Since remote sensing instruments typically have footprints of 100s to 1000s of meters, snow properties must be parameterized within the footprint. The default assumption of using the bulk average to estimate a geometric correction for the radar return breaks down for example when most of the snow mass is located at ridge sails and a large fraction of level ice areas is depleted in snow. We will explore possible additional sub-footprint parameterizations for remote sensing algorithm.

The same snow properties impact active microwave (CryoSat-2) and passive microwave (AMSR2, SMOS) sensors, although the effects vary depending on the wavelength, polarization and angle of the interrogating EM wave. A microwave can be scattered at the upper interface between air and snow, or by discrete layers within the snowpack. The degree of scattering increases as the horizontal scale of the interface roughness approaches the wavelength of the radiation, as the roughness increases, as the incidence angle of the wave approaches nadir, and as the dielectric contrast between air and snow widens (Hallikainen and Winebrenner, 1992).

A microwave can also be absorbed within the snow volume or scattered multiple times by individual snow grains. The degree of attenuation depends on the wavelength, snow grain size distribution and the snow dielectric constant, but has little dependence on wave polarization or incidence angle (Powell et al., 2006). The dielectric constant of snow depends weakly on the snow temperature, but

strongly on the presence of liquid water or brine within the snowpack (Hallikainen and Winebrenner, 1992). Consequently, surface and volume scattering generally increase over the winter to spring transition, as the snowpack starts undergoing freeze-thaw cycles (Langlois and Barber, 2007), and are higher over first-year sea ice where brine can be wicked up into the snow basal layers during ice formation (Nandan et al., 2017). Table1 summarizes these effects.

	Parameter	Estimated Importance		Scattering Mechanism
		Ku-band	Ka-band	
Snow	Air-snow interface roughness	Low	High	SS, R
	Snow temperature	Low	Low	VS
	Snow liquid water	High	High	VS
	Snow density	Med	Low	VS
	Snow grain size	High	High	VS
	Snow salinity	High	Low	VS
	Fresh ice lenses	Med	Med	VS, SS
	Snow depth	Med	Low	VS
Sea Ice	Snow-ice interface roughness	High	Low	SS, R
	Sea ice temperature	Low	Low	SS
	Sea ice salinity	Low	Low	SS
	Large-scale topography	High	High	SS, R

Table 1 – Geophysical factors controlling the volume scattering (VS), surface scattering (SS) and reflection (R) of radar waves from snow-covered sea ice at near-nadir incidence angles

Figure 9.1 illustrates the sensitivity of a modelled CryoSat-2 Ku-band SAR echo to several key snow properties: the grain size, density and depth (Landy et al., 2019). For typical air-snow interface roughness over sea ice of ~1 mm, surface scattering at Ku-band is low. At realistic snow grain sizes (> 0.5 mm), Mie-type scattering dominates absorption in dry snow at frequencies around 13 GHz and above (Winebrenner et al., 1992). Thus, snow volume scattering at Ku-band increases directly as a function of snow grain size, density of grains, and total snow depth; producing a characteristic broadening of the waveform leading edge (Figure 13.1).

By modelling the response of the CryoSat-2 echo to prescribed geophysical snow properties, the respective contributions to the total backscattered echo power of snow surface and volume scattering can additionally be decomposed (Landy et al., 2019; Figure 9.2). At Ka-band (36 GHz), for example for the AltiKa SARAL instrument, the volume scattering within the snowpack is larger than at Ku-band (Winebrenner et al., 1992). The theoretical e^{-1} penetration depth for Ka-band in dry snow is around 5 cm, in comparison to around 50 cm at Ku-band (Guerreiro et al., 2016).

Uncertainties in a few snow parameters can have a first-order impact on, for example, snow depth retrievals from passive microwave sensors or derived sea ice floe elevations from altimeters. Snow wetness and grain size (connected to temporal snow temperature variations) affect the accuracy of passive microwave snow depth algorithms, but Kern et al. (2019) suggest temporal averaging of brightness temperatures over a few days can reduce uncertainty.

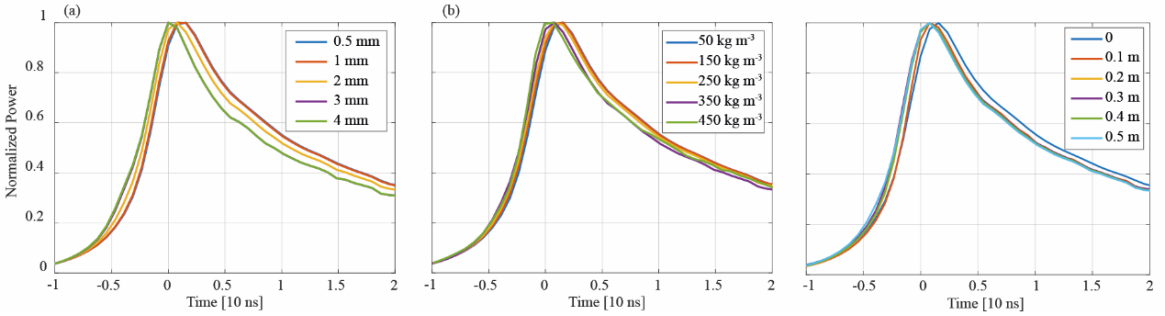

Figure 9.1 – Sensitivity of a modelled CryoSat-2 echo from sea ice to varied snow physical properties. (a) Grain size. (b) Density. (c) Depth. Assuming a single homogenous snow layer with bulk geophysical properties. From Landy et al. (2019).

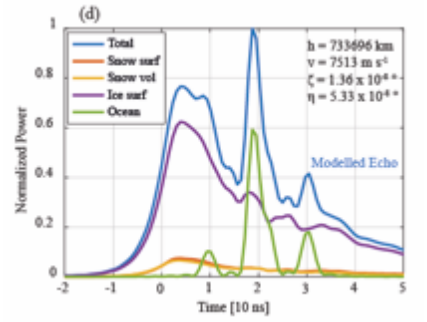

Figure 9.2 – Example of a CryoSat-2 echo modelled from real OIB sea ice surface topography and snow depth observations, including the total echo and the echo decomposed into contributions from (i) air-snow interface scattering, (ii) snow volume scattering, (iii) snow-ice interface scattering, and (iv) reflection from off-nadir leads. For this simulation, the snow depth was 20 cm and the snow density and grain size were estimated to be 350 kg m^{-3} and 1 mm, respectively. From Landy et al. (2019).

For altimeters such as CryoSat-2, the accuracy of measured sea ice floe elevations depends on the accuracy of the waveform retracking. The time t = 0 identifies the snow-ice interface (retracking point) in the waveform simulations in Figure 9. It is clear from these plots that significant variations in snow grain size and depth, can obscure the retracking point and reduce the accuracy of all types of retracking algorithm (heuristic or physical) (Kurtz et al., 2014; Landy et al., 2019). Studies disagree on the penetration depth of the Ka-band radar altimeter AltiKa into snow on Arctic sea ice (from near zero to 100% penetration) (Armitage and Ridout, 2015; Maheshwari et al., 2015; Guerreiro et al., 2016). Field observations from sea ice in the Arctic and Antarctic also demonstrate that the Ku-band CryoSat-2 may not fully penetrate the snowpack when highly metamorphosed layers or ice lenses are present (Willatt et al., 2011) or brine has been wicked into the snow basal layer (Nandan et al., 2017).

In multi-frequency snow products, another important source of uncertainty comes from the bias in the measured scattering surface from each radar altimeter as a function of the footprint geometry and the macroscopic snow and ice roughness within it. Modelling studies indicate that empirical thresholds and physical algorithms should realistically change depending on sea ice properties, principally surface roughness at the scale of the radar footprint (Kurtz, et al., 2014; Landy, et al., 2019). This combination of effects is illustrated on Figure 10 showing the perceived bias in differential penetration into the snow pack from Ka (AltiKa) and Ku band (CryoSat-2) radar altimeters operating in different modes (LRM for AltiKa vs SAR for CryoSat-2). To circumvent this roughness bias, Lawrence et al., (2018) proposed to use an empirical calibration approach against airborne data, Guerreiro et al., (2016) proposed to use a pseudo LRM mode (pLRM) for CryoSat-2 to facilitate the comparison with the LRM mode from AltiKa, while Landy et al. (2019) proposed instead to directly simulate the echo response function for different degrees of surface roughness and footprint geometries. In WP3, we will implement these approaches and compare the skill of the resulting snow products.

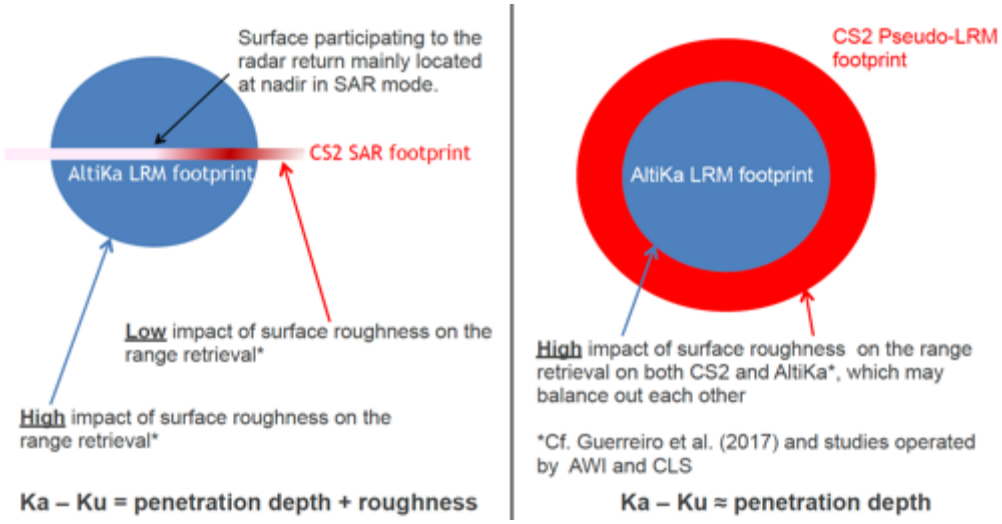

Figure 10 - Schematic illustrating the combine effect of penetration depth, roughness and footprint geometry on the measured differential penetration depth from radar altimeters. Credit: Cryo-SEANice project.

4.3. Radar freeboards uncertainty

Quartly et al. (2019) classified the waveform retracking methods over snow covered ice floes in terms of the mode of operation (LRM/SAR) and the type of the retracker used (empirical/physical). Table 2 summarizes the approaches used by our project partners together with their respective advantages and drawbacks.

Group	Retracker	Satellite	Mode	Comments	Reference
CPOM	TFMRA70 (empirical)	Envisat	LRM	Empirical biases (i.e. roughness, snow, scattering) (-) Fast (+) Calibrated (+)	Tilling et al. (in prep)
		CryoSat-2	SAR	Empirical biases (-) Fast (+) Calibrated (+) Product available (+) Product operational (+)	Tilling et al (2018) Lawrence et al. (2019)
AWI	TFMRA50 (empirical)	Envisat	LRM	Empirical biases (-) Fast (+) Calibrated (+) Merged with CS2 (+)	Paul et al. (2018)
		CryoSat-2	SAR	Empirical biases (-) Fast (+) Calibrated (+) Product available (+) Product operational (+) Merged with SMOS (+)	Hendricks et al. (2016) Ricker et al. (2017)
LEGOS	OCOG (empirical)	Envisat	LRM	Empirical biases (-) Fast (+)	Guerreiro (2016)
		CryoSat-2	pLRM	Empirical biases (-) Fast (+) Footprint consistent with LRM (+)	
	TFMRA70 (empirical)	Envisat	LRM	Empirical biases (-) Fast (+)	Guerreiro (2017)
		CryoSat-2	SAR	Empirical biases (-) Fast (+)	

	SAMOSA+ (analytical)	CryoSat-2 Sentinel-3	SAR	Physical retracker (+) Roughness (+) Gaussian (-) Slow (-) Snow biases (-) Scattering biases (-)	Laforge (2019)
FMI	TFMRA50 (empirical)	Envisat	LRM	Empirical biases (-) Fast (+) Calibrated (+) Merged with CS2 (+)	XX
UiT	FEBM LARM (numerical)	CryoSat-2	SAR	Physical retracker (+) Roughness (+) Lognormal (+) Slow (-) Snow biases (-) Scattering biases (-)	Landy et al (2019) Landy et al (in review)
		Envisat/AltiKa	LRM	Physical retracker (+) Roughness (+) Lognormal (+) Slow (-) Snow biases (-) Scattering biases (-)	Landy et al (private communication)
NASA	Physical (semi-analytical)	CryoSat-2	SAR	Physical retracker (+) Roughness (+) Gaussian (-) Slow (-) Snow biases (-) Scattering biases (-)	Kurtz et al (2014)

Table 2 - Radar freeboard algorithms implemented by groups of our consortium.

For **low resolution mode (LRM)** radar altimeters such as ERS1/2, Envisat and AltiKa, the most commonly used *empirical retracker* is the TFMRA (Threshold First Maximum Retracker Algorithm) for its ability to select the first local maximum instead of later peaks possibly contaminated by off-nadir reflections off leads. TFMRA is currently the algorithm implemented by our project partners at LEGOS (Guerreiro et al., 2017), AWI (Paul et al., 2018), and CPOM (Tilling et al., 2017) for estimating the radar freeboard from Envisat. Guerreiro et al. (2016) also used the OCOG (offset centre-of-gravity) algorithm to retrack waveforms from AltiKa (LRM) and CryoSat-2 (p-LRM, used to mimic the footprint characteristics of the LRM mode). More recently, project partners from UiT and UCL developed a *physical retracker* based on a forward model called FBEM (facet-based numerical echo model) to perform direct numerical simulations of waveform echoes from (Landy et al., 2019) and adapted it to retrack waveforms from LRM radar altimeters Envisat and AltiKa (Figure 11).

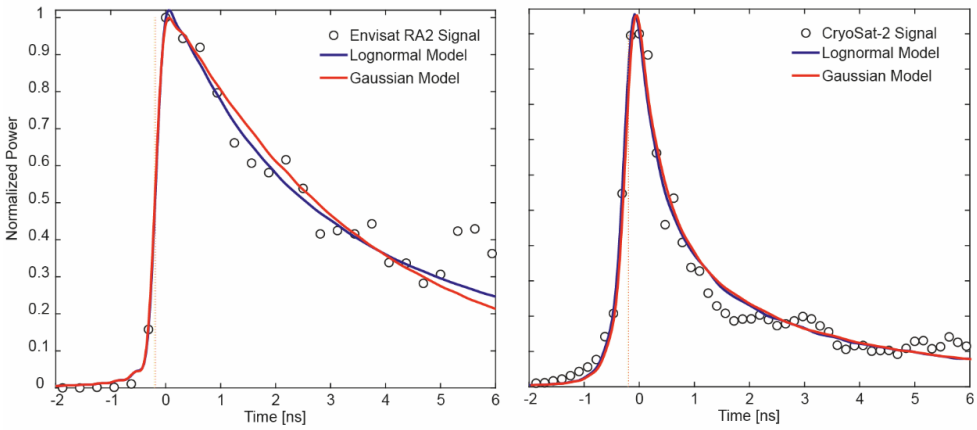

Figure 11 – Modelled (a) LRM and (b) SAR echoes from sea ice and fit to observed waveform signals from Envisat RA-2 and CryoSat-2, respectively, in March 2012. For each signal, two separate echoes have been simulated assuming the sea ice has large-scale roughness characterized by a (i) Lognormal and (ii) Gaussian statistical distribution. The derived sea ice roughness is almost the same between signals in (a) and (b). Courtesy of J. Landy.

For **delay-Doppler (SAR)** radar altimeters such as CryoSat-2 or Sentinel-3 A/B, the *empirical* TFMRA is the retracker of choice for several groups with various thresholds being used. CPOM (Lawrence et al., 2019; Tilling et al., 2017) and LEGOS (Guerreiro et al., 2017) use a 70% threshold for the retracking point, and AWI 50% (Paul et al., 2018). Some groups use different retracking algorithms for sea ice floes and leads, in which case a constant bias correction is applied to align the retrieved sea ice

elevation and sea level (Tilling et al., 2017). Project partners from NASA Goddard have implemented a physical waveform retracking (Kurtz et al., 2014). The SAMOSA (Ray et al., 2015) and SAMOSA+ (Dinardo et al, 2017) SAR waveform models also belongs to the category of models with analytical solutions. Our LEGOS partners (Laforge et al, in review) quantified the differences between empirical (TFMRA) and physical (SAMOSA+) retrackers and found the latter to provide more accurate freeboard estimations. Landy et al., (2019) (UiT and UCL PPs) implement a direct numerical simulation approach to simulate CS2 SAR waveforms that relax the Gaussian approximation of the surface topography (Figure 19). The same authors used this Lognormal Altimeter Retracker Model (LARM) to derive sea ice freeboard (Landy et al, in review) and compared it with various physical and empirical other products to demonstrate that all retrackers produce diverse solutions for the radar freeboard derived from CryoSat-2 (Figure 12).

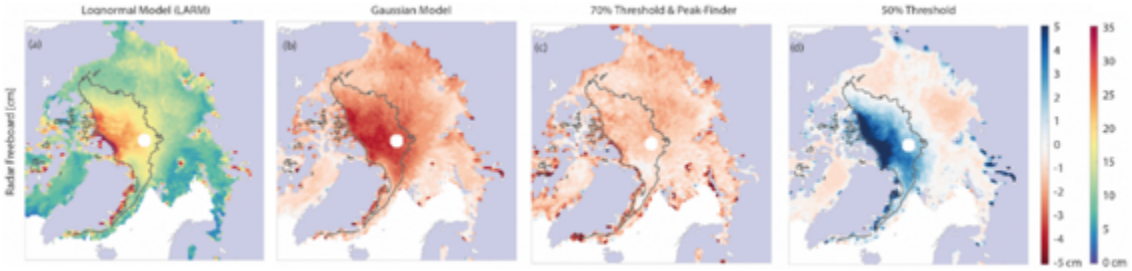

Figure 12 – March mean CryoSat-2 radar freeboard [cm] obtained from (a) the Lognormal Altimeter Retracker Algorithm (LARM). Differences between each retracker and LARM are shown for the Gaussian model (b) the TFMRA70 Model, and (c) the TFMRA50 model. The MYI edge is highlighted in grey. Figure adapted from Landy et al. (in review).

We now discuss the methods proposed to retrieve the sea ice and snow freeboards along with the corresponding bias corrections and calibrations techniques that need to be applied to the radar freeboard.

4.4. Retrieving snow and ice freeboards

We will retrieve snow thickness as a combination of radar freeboards using two methodologies described in WP1, namely an empirical **calibration technique** and a **bias correction technique**. The former is inspired by the approach taken in Lawrence et al. (2018) while the latter is more in line with Guerreiro et al. (2016) (both PP in this project). Both techniques rely on the assumption that the different radar penetration into the snow pack at two separate frequencies holds some information as to the snow thickness over the sea ice.

For a radar altimeter, the equation relating the radar freeboard, F_R, to the sea ice freeboard, F_I, snow thickness, H_S, and penetration factor, α, can be written for CryoSat-2:

$$F_R^{CS2} = F_I + \left(1 - \alpha^{CS2}\,\frac{c}{c_s}\right) H_S,$$

where we have accounted for the delayed propagation of the radar wave into the snow pack at a speed, c_s, as opposed the propagation speed into vacuum, c.

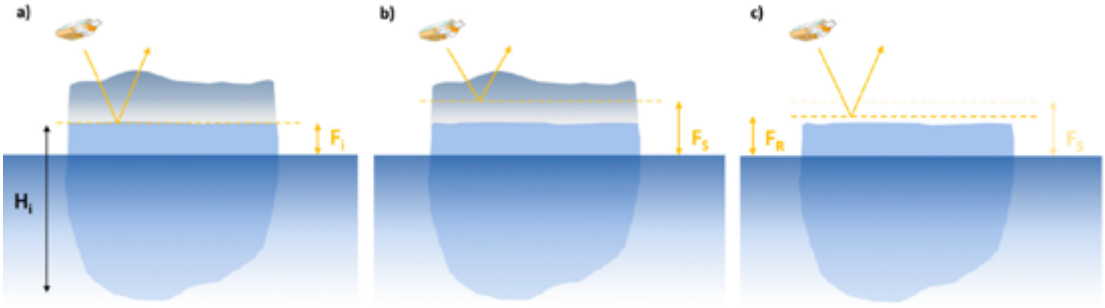

Figure 13 - Schematic showing the snow (or laser) freeboard (a), scattering horizon (b), and radar freeboard (c) for CryoSat-2.

The same equation for AltiKa can be expressed in the same way as:

$$F_R^{AK} = F_I + \left(1 - \alpha^{AK} \frac{c}{c_s}\right) H_S.$$

By simply subtracting these two equations one can then find a simple expression of the snow thickness as a function of differences of radar freeboard and penetration factors:

$$H_S = \frac{F_R^{AK} - F_R^{CS2}}{\alpha^{CS2} - \alpha^{AK}} \cdot \frac{c_s}{c} = \frac{\Delta F_R}{\Delta \alpha} \cdot \frac{c_s}{c} = \frac{\Delta F_R}{\Delta \alpha} \cdot 0.781.$$

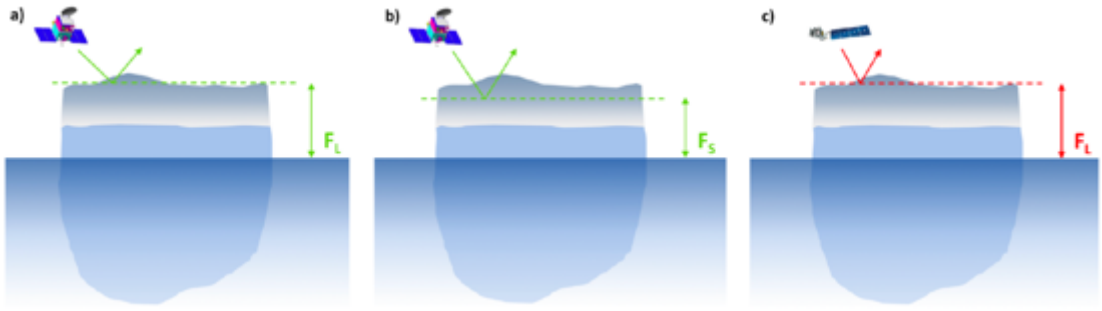

Figure 14 – Schematic showing the snow (or laser) freeboard (a), scattering horizon (b) for AltiKa, and snow (or laser) freeboard for a ICESat-2 (c).

In the **bias correction technique** as implemented by Guerreiro et al. (2016), the traditional assumptions of perfect penetration at Ku-band for CryoSat-2 (i.e. $\alpha^{CS2} = 1$) and no penetration at Ka-band for AltiKa (i.e. $\alpha^{AK} = 0$) were made and the snow thickness given as $H_S = 0.781\ \Delta F_R$. Guerreiro et al. (2016) only accounted for inter-mission footprint biases by using a pLRM version of CS2 and in the future more advanced radar echo models (i.e. Landy et al. 2019) can be used to account for roughness biases, snow and volume scattering biases, as well other biases due to the snow vertical structure (i.e. salinity, liquid layers, etc). Furthermore, such physically based models can be extended to simulation of airborne radar echoes and allow for a more rigorous validation of the snow products.

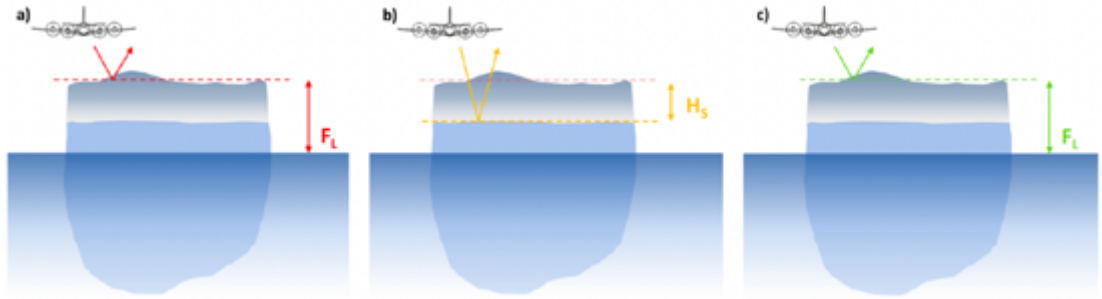

Figure 15 - Schematic showing the snow (or laser) freeboard from OIB ATM (a), snow thickness from OIB snow radar (b), and snow (or laser) freeboard from Karen (c).

In the **calibration technique** by Lawrence et al. (2018) on the other hand, perfect knowledge of radar freeboards and penetration is not assumed and instead the authors use an empirical regression of the satellite radar freeboard against OIB airborne radar and laser freeboards (Figure 15) as a function of satellite pulse peakiness as shown in Figure 16 such that the snow thickness is given by:

$$H_S = F_R^{AK} + \Delta f_{AK}(PP_{AK}) - F_R^{CS2} - \Delta f_{CS2}(PP_{CS2}).$$

This methodology is empirical and can be applied to any radar freeboard provided as input to the algorithm. Note that Laforge et al. (in review) compared radar freeboards retrieved from an empirical (TFMRA) and physical retracker (SAMOSA+) and proposed a similar calibration approach as a function of pulse peakiness. As can be seen in Figure 12 radar freeboards provided by different groups will differ from each other significantly and this calibration methodology against a common airborne dataset allows to simply account empirically for all biases. Pros and cons of both methods are summarized in Table 9. The major disadvantage of the bias correction method, as currently applied, is that it assumes

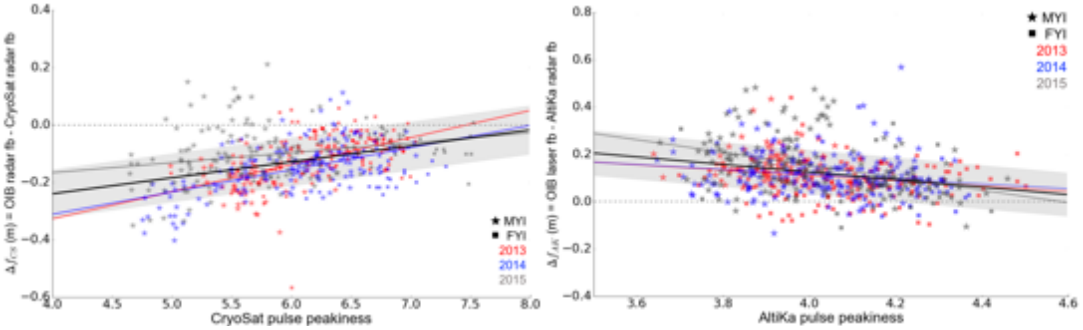

Figure 16 – Left: Calibration curve of CS2 radar freeboard against OIB radar freeboard as a function of CS2 pulse peakiness. Right: Calibration curve of AK radar freeboard against OIB laser freeboard as a function of AK pulse peakiness (Lawrence et al., 2018).

perfect penetration at Ku-band and no penetration at Ka-band, relying on the comparison of LRM to LRM footprints to remove all biases. The major disadvantage of the calibration method, as currently applied, is that it relies on empirical calibration to an OIB airborne dataset that is strongly biased towards the end of the Arctic spring (Mar-Apr).

Method	Formula	Pros and Cons
Bias correction	$H_S = \frac{F_R^{AK} - F_R^{CS2}}{\alpha^{CS2} - \alpha^{AK}} \cdot \frac{c_s}{c}$	(+) method is physically based (+) remove known biases (+) accounts for roughness and footprint shape (+) can incorporate surface and volume scattering models (+) can be applied to airborne radar model for validation (-) model dependent (-) computationally heavy (-) requires simplifying assumptions
Calibration	$H_S = F_R^{AK} - F_R^{CS2} + \Delta f_{AK}(PP_{AK}) - \Delta f_{CS2}(PP_{CS2})$	(+) method applies to all radar freeboard (+) makes no physical assumptions (+) accounts for varying penetration factors (+) (-) empirical (-) relies on airborne data (-) location and season dependent (-) cannot adjust to changes of climate and surface characteristics (-) can lead to misinterpretation of data (-) errors on freeboard products accumulate

Table 3 – Summary of bias correction and calibration algorithms with corresponding formulas and relative of both methods.

As a final contribution to the bias correction algorithms we will use our newly developed technique using **artificial intelligence (AI)** to classify and retrack the radar altimetry echoes (Landy et al, 2019). More specifically and as illustrated in Figure 17, the CryoSat-2 echoes can be matched using a **machine learning** classifier to the best fitting FBEM model generated echoes. This type of approach can be extended to all types of surfaces, footprint configurations, and altimeters (including ICESat-2).

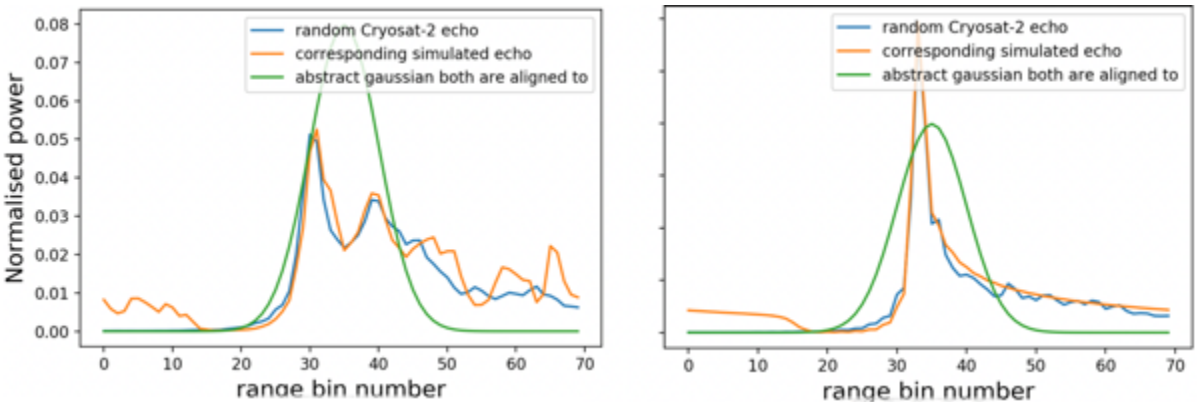

Figure 17 – Two example of real CryoSa-2 echoes (blue) fitted to a best model FBEM echoes (orange) for two different level of surface roughness and lead geometries. The green Gaussian is here for alignment purposes only. Credit: M. Tsamados, J. Landy and C. De Rijke-Thomas.

4.5. Error analysis

Preliminary work in collaboration with CLS as part of the ESA PolarIce project providing scientific expertise for the future CRISTAL mission has proposed a first decomposition of the different contributing terms in the snow error analysis together with the correlation length scales and time scales of each of these error terms. A summary of these preliminary results is shown in Table 4.

	Decription of the errors	Error	Correlation length	Correlation time
Radar freeboard CryoSat-2 (Ku)	SLA interpolation error	4-6 cm (FYI) 8-12 (MYI)	200 km	0
	Errors induced by the surface roughness or snagging biases	5-10 cm	< 1 km	0
Radar freeboard AltiKa (Ka)	SLA interpolation error	6-10 cm	200 km	0
	Errors induced by the surface roughness or snagging biases	5-10 cm	< 1 km	0
Snow penetration (Ku)	Penetration error: Salinity effect Ice layering Surface melt Grain size, snow density, etc	~10 cm <5cm seasonal seasonal seasonal	~1000 km <1000 km “ “ “	~ month “ “ “ “
	Speed of light correction	2-4 cm	~2000 km	~ month
	Errors induced by the surface roughness or snagging biases	~10 cm (negative bias on freeboard)	< 1 km	0
Snow penetration (Ka)	Penetration error: Salinity effect Ice layering Surface melt Grain size, snow density, etc	~5 cm <1 cm < 1 cm < 1 cm < 1 cm	~1000 km <1000 km “ “ “	~ month “ “ “ “
	Speed of light correction	< 2 cm	~1000 km	~ month
	Errors induced by the surface roughness or snagging biases	5-10 cm	< 1 km	0

Table 4: Snow thickness error analysis. Credit: PolarIce project (CRISTAL PhaseA/B1).

Preliminary analyses of the spatial and temporal length scales of the sea level anomaly (SLA) obtained from lead returns with CryoSat-2 are shown in Figure 18, averaged over the full CryoSat-2 record. These plots demonstrate that sea surface heights have widely different scales of correlation across the Arctic basin.

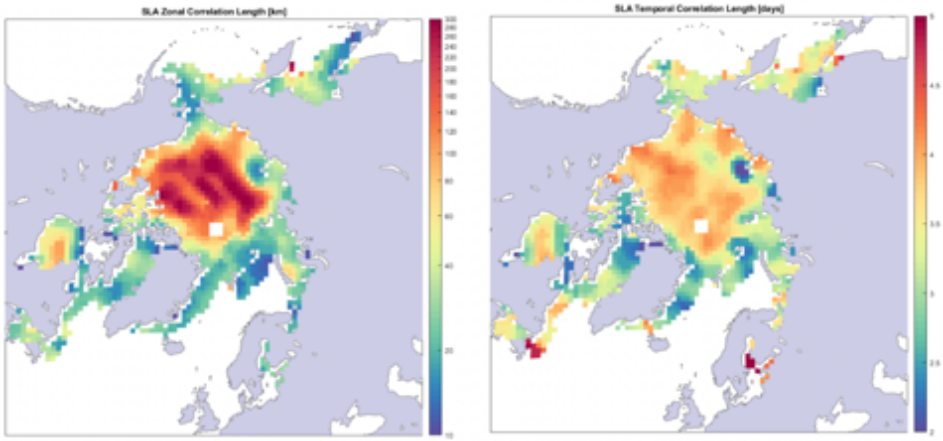

Figure 18 – Zonal [km] and temporal [days] correlation length scales of the Arctic sea level anomaly (SLA), averaged over all winter months of the CryoSat-2 record. Credit, J. Landy.

For each of the two snow thickness formulas shown in Table 4 we will perform an error analysis following the methodology suggested by the authors of the corresponding studies.

Lawrence et al. (2018) propose a simple error propagation analysis:

$$\sigma_{h_s} = 0.781\Big(\sigma^2_{f_{AK}} + \sigma^2_{\Delta f_{AK}} + \sigma^2_{f_{CS}} + \sigma^2_{\Delta f_{CS}} + 2\sigma_{f_{AK}\Delta f_{AK}} - 2\sigma_{f_{AK}f_{CS}} - 2\sigma_{f_{AK}\Delta f_{CS}} - 2\sigma_{\Delta f_{AK}f_{CS}} - 2\sigma_{\Delta f_{AK}\Delta f_{CS}} + 2\sigma_{f_{CS}\Delta f_{CS}}\Big)^{\frac{1}{2}},$$

where the first where the first four terms are the errors on the four variables of equations shown in Table 3 and the last six terms are the covariances between them. The authors find that error on monthly-gridded freeboards is dominated by the uncertainty on the interpolated sea-level anomaly (SLA), calculated from the SLAs of waveforms identified as leads (Tilling et al., 2017). Since the interpolation is performed along-track, separate satellite passes over each grid cell over the month are decorrelated, and thus the error is minimised by $1/\sqrt{N}$, where N is the number of passes over a grid cell in one month (see Figure 19). The overall budget error for the snow thickness is shown on Figure 19 for two different grid resolutions with values in the 8-10 cm range for the (1.5 lon x 0.5 lat) grid and 4-6 cm range for the (6 lon x 3 lat) grid. These estimates compare well with the standard deviation between the dual frequency satellite estimates and the airborne snow values as shown on the scatter plot of Figure 16.

Guerreiro et al. (2016) uses CS2 and AK crossover analysis to show that individual radar freeboard (elevations) uncertainties do not exceed 2-3 cm and therefore the analysis of the surface position difference at CryoSat-2/AltiKa crossovers can provide retrieval of large-scale snow depth with a relatively high accuracy. The authors further use comparison with airborne and in-situ snow data to estimate the snow uncertainty at the 5-6 cm level. Another aspect to consider on the snow thickness error is the availability of recent and interesting airborne data using Ku and Ka radar measurements in the Arctic region from the 2017 Cryovex campaign (Ricker et al. AGU 2018 poster). We discuss this further in WP4.

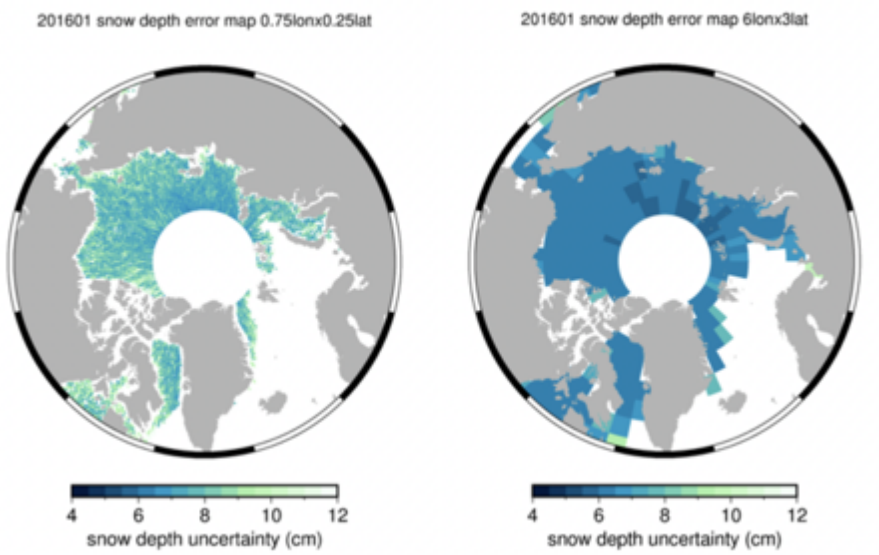

Figure 19: Snow depth error maps for different grid resolutions. Left: (1.5 lon x 0.5 lat) grid. Right: (6 lon x 3 lat) grid. Credit: Isobel Lawrence.

At the LEGOS, the approach is to consider uncertainties globally. Uncertainties are calculated from the along track variability of the sea level anomalies calculated in leads (within 25 km sections). Uncertainties are calculated assuming that errors are unbiased, uncorrelated and follow a gaussian law. We can then apply the following Gaussian propagation law: $\varepsilon^2_{f(x_i)} = \sum_{i=1}^{n} \left(\frac{\partial(f(x_i))}{\partial x_i}\right)^2 \varepsilon^2_{x_i}$

Uncertainties on the radar freeboard are then $\epsilon_{fb_{radar}} = \sqrt{\varepsilon^2_{H_{floe}} + \varepsilon^2_{H_{lead}}}$

The uncertainty attributed to individual surface height measurements can be estimated from the local (i.e. within along-track sections of 25 km) standard deviation of surface heights. Regarding the ice floes, the surface height standard deviations are strongly impacted by the freeboard variability and can therefore not be used to estimate uncertainties. The assumption is that the individual uncertainty of surface height over ice floes is identical to the individual uncertainty over leads. Uncertainties of leads and floes is then:

$\varepsilon^2_{H_{floe}} = \frac{{\sigma_{SLA}}^2}{N_{floe}}$ $\varepsilon^2_{H_{lead}} = \frac{{\sigma_{SLA}}^2}{N_{lead}}$ with N_{floe} and N_{lead} are the number of floes and leads within each section of 25 km. Using the equations detailed in the previous section, we make the assumptions of no penetration for the ka band and a total penetration for Ku band. Following Kwok & Cunningham (2015) the ratio $\frac{c_s}{c}$ is given by $\frac{c_s}{c} = (1 + 0{,}51 \times \rho_s)^{(-1{,}5)}$

Then, the snow depth is then $sd = (fb_{ka} - fb_{radarku}) \times (1 + 0{,}51 \times \rho_s)^{(-1{,}5)}$ and the snow depth uncertainty ϵ^2_{sd} is then given by

$$\epsilon_{sd}^2 = \left(\sqrt{\left(\epsilon_{fb_{ka}}^2 + \epsilon_{fb_{ku}}^2\right)} \times (1 + 0{,}51 \times \rho_s)^{(-1,5)}\right)^2 + \left((fb_{ka} - fb_{radarku}) \times (-1{,}5) \times 0{,}51 \times (1 + 0{,}51 \times \rho_s)^{(-2,5)} \times \epsilon_{\rho_s}\right)^2$$

Note that ρ_s is given by the Warren Climatology.

In this study we will investigate the impacts of these 2 methods (LEGOS vs UCL) in order to define an optimal approach to characterize uncertainties in further snow depth products.

4.6. Laser freeboard and snow uncertainties

ICESat had a ~70m diameter footprint, so biases due to footprint size or retracking method are presumed negligible and the instrument is assumed to offer accurate estimates of the snow freeboard. Note that because ICESat and OIB did not overlap in time it is not possible to calibrate the laser snow freeboard against airborne data.

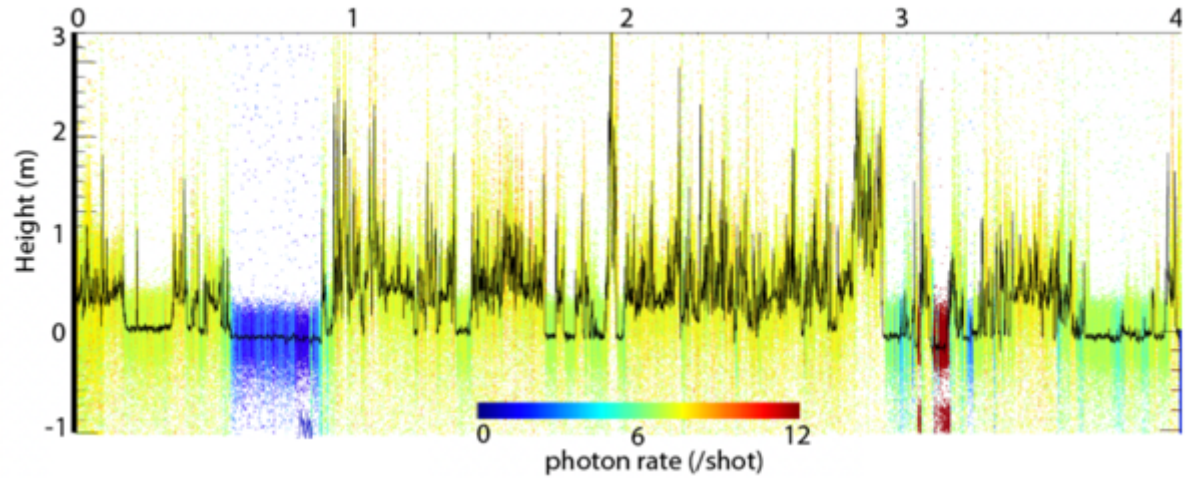

Figure 20 -Along-track surface height profiles and related parameters from a strong ATLAS beam. Color of photons is the average rate of given 150-photon height segment (Kwok et al, 2019).

ICESat-2 has 3 pairs of beams, each separated across track by 3.3 km, with a footprint of ~17m. Recent analysis (Kwok et al, 2019) has shown that along-track height precision of ~2cm is achievable and that quasi-specular returns (crucial for freeboard calculations) are detectable in openings as narrow as ~30m. In this project we will start by using the ATL07 and ATL10 NASA products (see in depth description in the IS2 ATBD) that contain profiles of surface heights and sea ice freeboards. The surface heights in ATL07 are derived from the height distribution of 150 photons that is modelled as the convolution of the ATLAS system impulse response with a Gaussian height distribution of width w. Along-track freeboards are calculated in consecutive 10-km segments as the difference of the snow elevation heights in ATL07 and the local estimates of sea surface.

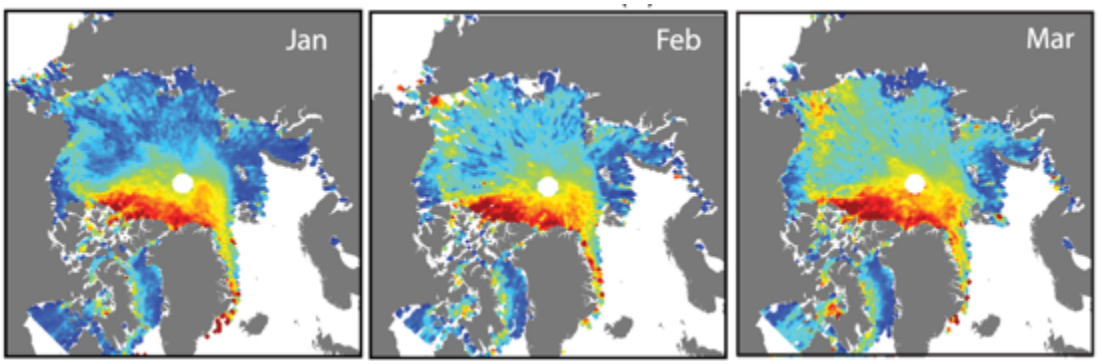

Figure 21 - Total radar freeboard retrieved by IS2 for Jan - Mar 2019 (Kwok et al, 2019).

The approach proposed by Lawrence et al. (2018) and Guerreiro et al. (2016) can both be reproduced to the radar – laser case and the corresponding equations can be re-written for the bias correction method as:

$$H_S = \frac{F_L^{IS2} - F_R^{CS2}}{\alpha^{CS2} - \alpha^{IS2}} \cdot \frac{c_s}{c},$$

and for the calibration approach as:

$$H_S = F_L^{IS2} + \Delta f_{IS2}(\rho_{IS2}) - F_R^{CS2} - \Delta f_{CS2}(PP_{CS2}),$$

where we have replaced the AK radar freeboard by IS2's laser freeboard, F_L^{IS2}, and where the dependence on the calibration function for the laser altimeter is now a function of the surface roughness, ρ_{IS2}, instead of the pulse peakiness.

To demonstrate the applicability of the calibration method to any two pairs of altimeters (including a radar-laser pair), the method was applied to the ICESat and Envisat satellites, whose periods of operation overlapped between 2003 and 2009 (Lawrence et al. 2018). Following the procedure outlined in WP3.1.1 of the proposal, Envisat freeboard was calibrated to the snow/ice interface. Envisat has a larger footprint than AltiKa, nominally 2-10km diameter (Connor et al., 2009). As such, the waveform returns are more often classified as ambiguous (showing a complex mixture of scattering behavior) and discarded. As a result, Envisat data are sparsely populated and in order to have sufficient coverage for comparison with OIB data and 50 or more points per grid cell (to reduce speckle noise), it was necessary to increase both the grid resolution and time window as compared with the calibration procedure performed for AltiKa and CS-2.

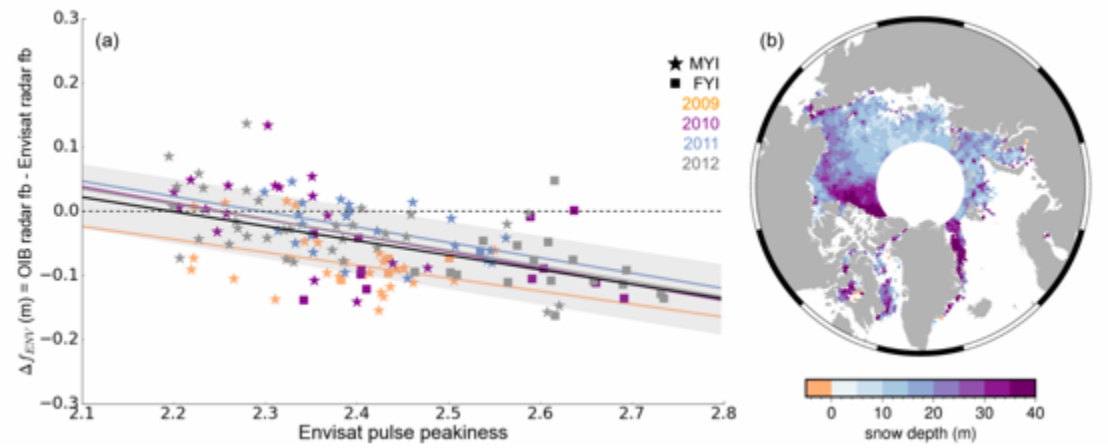

Figure 22 - Envisat calibration relationship, derived from comparison of coincident OIB and Envisat data. Data and corresponding linear regression fits for 2009, 2010, 2011 and 2012 and shown in orange, purple, blue and grey respectively. Star and square symbols represent multi-year and seasonal ice respectively. (b) Snow depth for ICESat's '3E' laser period (22nd February 2006 to 27th March 2006), retrieved by subtracting calibrated Envisat freeboard from ICESat freeboard and multiplying by a factor 0.781.

Satellite data for the +/-15 days surrounding each 2009-2012 OIB campaign day were averaged onto a 3° longitude x 0.75° latitude grid. $\Delta f_{ENV}(PP_{ENV})$, defined as OIB radar freeboard minus Envisat freeboard, plotted against Envisat pulse peakiness, PP_{ENV}, is shown in Figure 22. The combined (all years) linear regression fit is shown by the black line. The shaded area shows the 68% prediction interval about the CLRF, corresponding to a +/-5 cm standard error (SE) of Δf_{ENV}. The snow thickness retrieved by subtracting calibrated Envisat freeboard from ICESat freeboard is show in Figure 34 for the ICESat laser period '3E' (22nd February 2006 to 27th March 2006). Snow depth spatial distribution follows the expected pattern of thicker snow (30 to 40 cm) over multi-year ice to the north of the Canadian Archipelago and in the Fram Strait, and thinner snow cover (<20cm) over the seasonal ice. Overall higher magnitudes as compared with March 2016 could be the result of a decline in multi-year ice fraction and precipitation over the past decade. Though validation is required, the result demonstrates the viability of combining laser and calibrated radar freeboard to retrieve snow depth. Recent validation of the total freeboard from IS2 against the total freeboard measured with OIB's ATM confirm their excellent match and the validity of the hypothesis made in Lawrence et al (2018) that both laser altimeters and airborne ATM measure the same top of the snow interface to within 2-4 cm (Kwok et al, 2019b).

5. IDENTIFICATION OF KEY TEST AREAS

5.1. Summary of inputs, tasks and outputs

Inputs required to Start:
• SoW [EOP-SDR/SOW/087-17/DFP]
• Proposal [UCL-PRO-19-MT1]
Task Description:
• Review validation datasets
• Identify candidate test area
Outputs:
• Catalogue of available, appropriate datasets
• Contribution D1: Requirement Baseline (RB)

5.2. Validation datasets

Our choice of key test areas is partially informed by the availability of good validation datasets. We describe these first here.

5.2.1. Airborne datasets

CryoVex and CryoVal

The main goal of the CryoVex/CryoVal campaigns is to quantify the accuracy with which CryoSat-2's SIRAL altimeter measures sea ice thickness, as well as investigating methods of improving the CryoSat-2 retrieval results. During the campaign a variety of ice regimes and thicknesses are sampled allowing researchers to assess the thickness retrieval performance of CryoSat-2 over a wide range of ice conditions. The campaign activities largely focus on collecting overlapping airborne radar and laser altimeter swaths across the sea ice (Figure 23). The field experiments have varied year to year, but have included airborne data gathered with the ASIRAS (Airborne SAR/Interferometric Radar Altimeter System) instrument in addition to field measurements, EM bird and ground penetrating radar (GPR) studies. Corner reflectors have been deployed to provide a height reference for interpreting the ASIRAS data. ASIRAS and the GPR operate over the Ku-band (13.5 GHz), the same central frequency as CryoSat-2, but with wider bandwidths which provide greater vertical resolution which can allow the air/snow and snow/ice interfaces as well as features within the snow pack to be resolved.

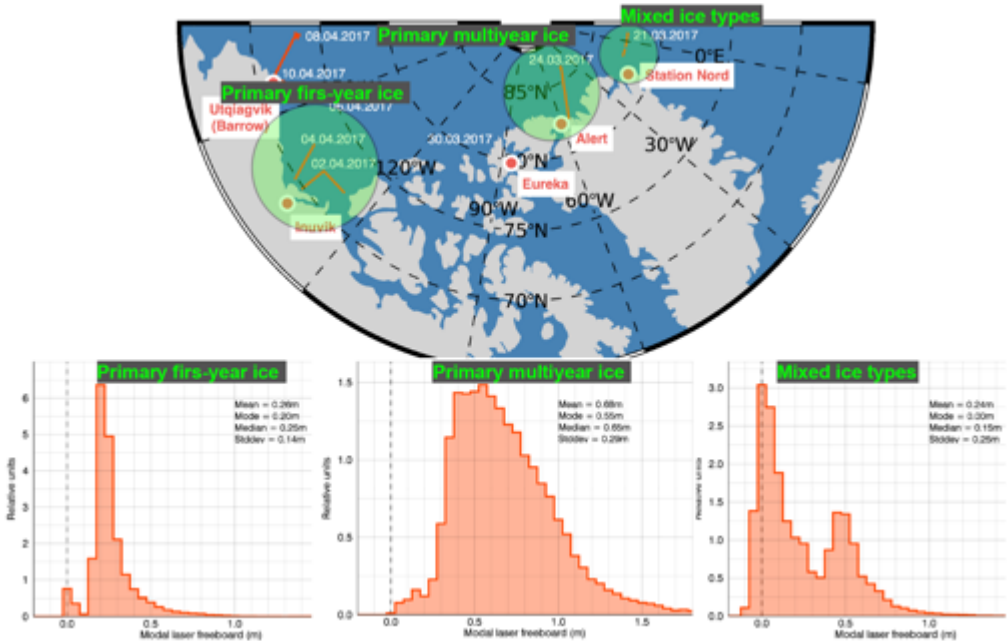

Figure 23 - Schematic showing recent CryoVex and other airborne validation campaigns in the Arctic. The distribution of laser freeboards show the differences over different ice type scenarios that will be used for validation purposes. Credit: AWI.

NASA Operation IceBridge (OIB). NASA have been monitoring sea ice in the Arctic and Antarctic with a suite of airborne instruments from 2009 to 2019, as part of their Operation IceBridge (OIB) Campaign (Figure 23). Relevant available datasets for this proposal include raw observations of snow and sea ice properties from multiple radar instruments (FMCW 2-8 GHz and Ku-band 13 GHz sensors), a laser scanner (ATM) and aerial photography (DMS). Additionally, OIB produce a derived sea ice data product from a combination of these instruments, offering snow depth and ice thickness estimates (with uncertainties) at 40 m spacing along the aircraft track. A majority of OIB campaigns cover the Central Arctic Ocean (Lincoln Sea), Beaufort Sea and Chukchi Sea in spring (Mar-Apr) (see Figure); however, a few campaigns are available for fall months (Oct-Nov). Our project partners at NASA GSFC have led the development of sea ice data products from OIB (Kurtz et al., 2013) and have developed algorithms for analysing sea ice topography from OIB (Petty et al., 2016). Our team have additionally used OIB to characterize the statistical and radar backscattering properties of air-snow and snow-ice interface roughness (Landy et al., In Review). A Sea Ice Freeboard, Thickness and Snow Depth Quick Look product is produced and archived at the National Snow and Ice Data Centre: (https://nsidc.org/data/docs/daac/icebridge/evaluation_products/sea-ice-freeboard-snowdepth-thickness-quicklook-index.html) (Kurtz et al., 2013), and will be used as part of WP4.

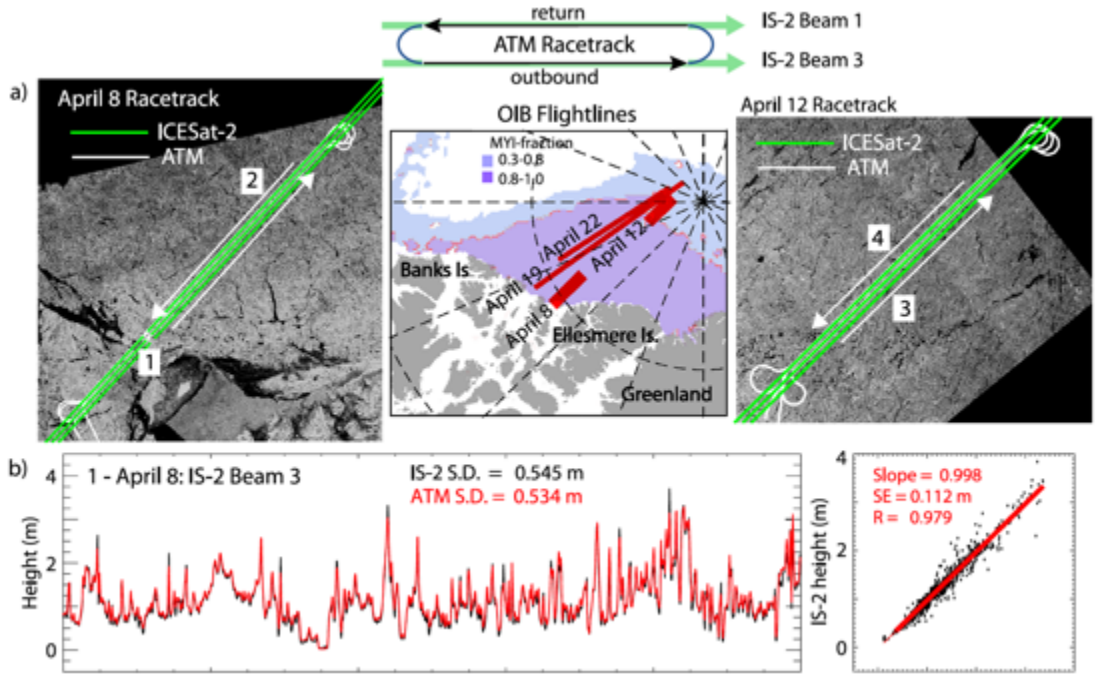

Figure 24 - Comparison of IS-2 and ATM surface heights in 10-km segments. (a) Location of the four OIB flight tracks (middle panel) and with the two racetracks (8 April: left panel; 12 April: right panel) overlaid on synthetic aperture radar imagery. (b) Along-track surface profiles (10-km segments) and scatterplots with regression results (slope, correlation, and standard error) for a sample segment along the flight tracks on 8 April (Copernicus Sentinel Imagery 2019, processed by ESA, archived at the Alaska Satellite Facility). ATM = Airborne Topographic Mapper; OIB = Operation IceBridge; ICESat-2 = Ice, Cloud, and Land Elevation Satellite-2 (Kwok et al, 2019).

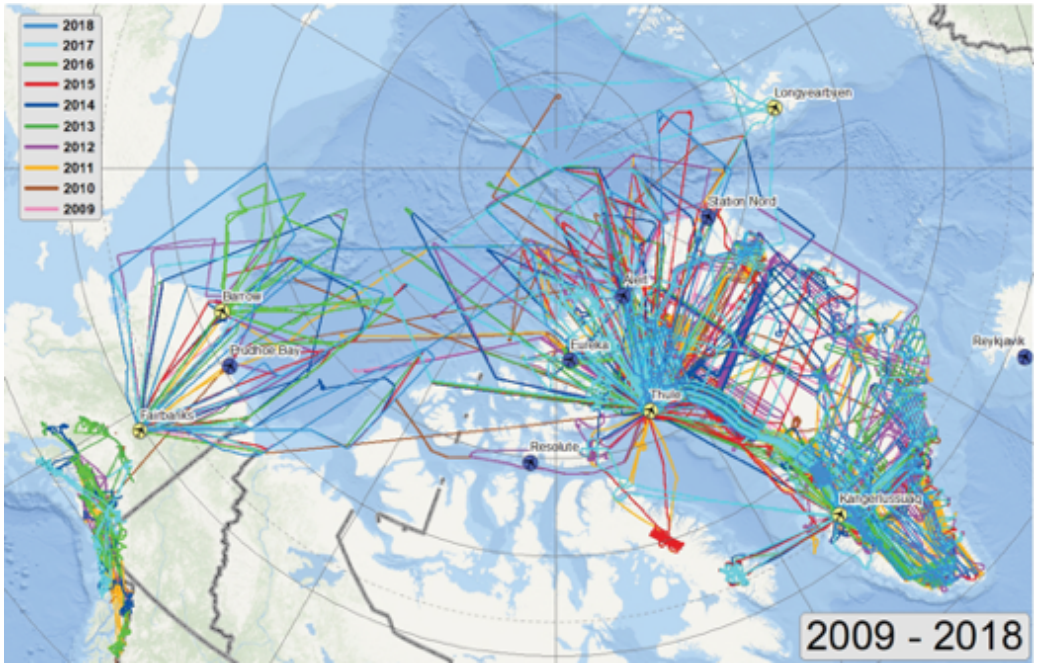

Figure 25 -2009-2018 Operation IceBridge flight lines. Credit: NASA.

AWI IceBird. The AWI IceBird campaign series (https://www.awi.de/en/science/climate-sciences/sea-ice-physics/projects/ice-bird.html) includes airborne observations of sea-ice thickness and surface properties during winter and summer. IceBird is based on the heritage of earlier PAMARCMIP campaigns with a central focus on EM-based total (sea-ice plus snow) thickness observations. The winter implementation since 2017 additionally includes a CRESIS snow radar (Jutila et al., 2021a) in combination with an airborne laser scanner. This sensor combination allows a full characterization of freeboard, snow depth and sea-ice thickness (Jutila et al. 2021b) and high spatial resolution and has collected (Figure 26). AWI IceBird data sets are available, respectively submitted, at the PANGAEA data base and can be found by filtering for the project 'AWI_IceBird'.

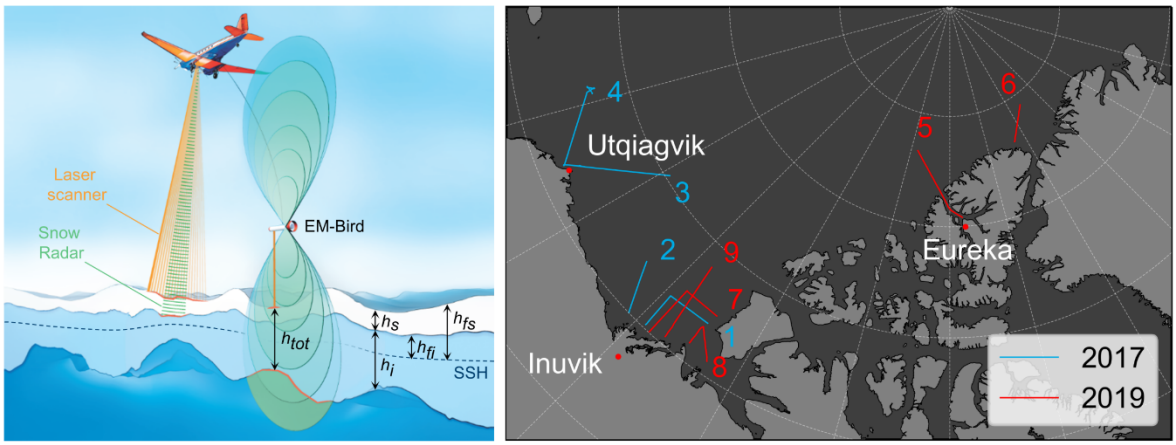

Figure 26: (left) Sensor configuration of the AWI IceBird Winter campaign including an ice thickness sensor (EM-Bird) in combination with a snow radar and a laser scanner. (right) surveys with simultaneous data collection of all three sensors during the two campaigns in 2017 and 2019. (source figures: Jutila et al. 2021b)

5.2.2. In-situ datasets (ASPeCt, MOSAiC , IMBs, and Snow buoys)

ASPeCT

In-situ data will be collected for sea ice and snow thickness validation as well as for investigation of radar penetration depth. Following Ozsoy-Cicek (2013), sea ice thickness, snow depth and freeboard data (as well as snow and sea ice densities) from the ASPeCt program (http:aspect.antarctica.gov.au/) will be compiled and analysed to assess and refine the empirical relationships found between total freeboard and sea ice thickness as proposed in Kern et al. (2015).

MOSAiC

The MOSAiC ice drift campaign (September 2019 – September 2020) will provide a unique opportunity for validating our snow depth products in regions not sampled by OIB (e.g. the eastern Arctic) and throughout a full annual cycle. This experiment aims to characterise the spatial and temporal variability of Ku- and Ka-band radar penetrations into snow on multi-year and first-year ice through gathering data from a static location (relative to the sea and ice) over a period of time, and gathering data along transects. A dedicated dual-radar study is being deployed during the MOSAiC experiment, using in-situ and on-aircraft Ku-Ka band radar to quantify radar backscatter at each frequency together with snow depth and ice thickness measurements. The PI and several partners for this proposal are involved with the MOSAiC mission and will have access to all in-situ data gathered over the campaign.

IMBs

The Ice Mass Balance buoys data (Richter-Menge et al*, 2006*) is monitored by the CRREL-Dartmouth Mass Balance Buoy Program with the goal of being a component of "a sustainable Arctic observing network". It provides point measurement of the ice mass balance characterized by a combination of snow and ice condition. The IMB Snow depth data are available at http://imb-crrel-dartmouth.org/archived-data/ and cover the entire 2013-2018 period in various location in the Arctic.

Snow buoys

Buoys are a source of continuous observations in a Lagrangian reference frame (Figure 27). A buoy dedicated for measurements of snow depth of sea ice has been developed by the Alfred Wegener Institute and deployed on sea ice in both hemispheres since 2013. The data is publicly available at the data portal of the meereisportal.de initiative. In the Arctic, the deployment strategy has a focus on initial deployment in the source regions of the Transpolar Drift, thus providing a snow depth information along trajectories from the Laptev Sea to Fram Strait. In the southern hemisphere, deployments are limited to the Weddell Sea.

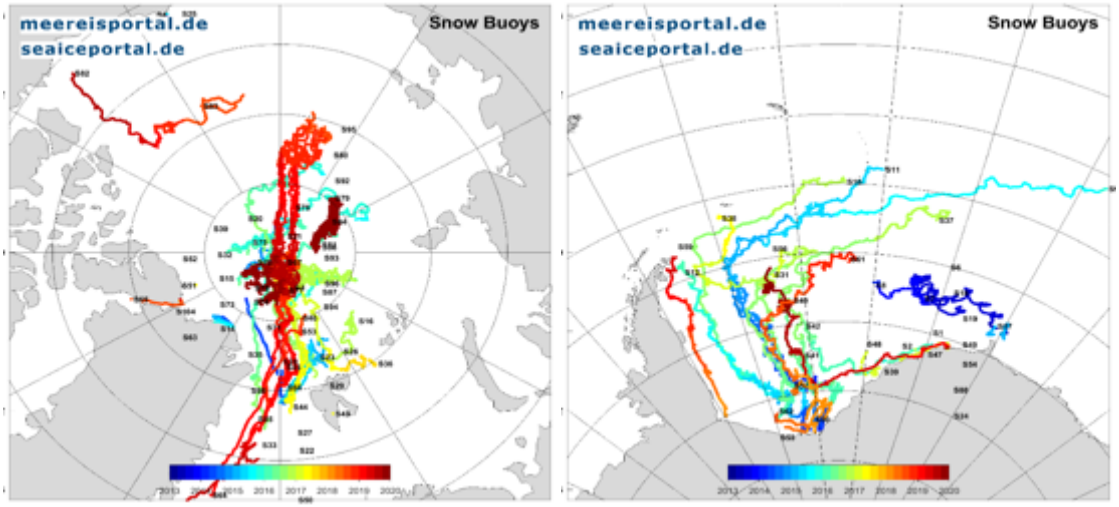

Figure 27: Drift tracks of snow buoys deployed in the Arctic (left) and Antarctic (right) color-coded by year of deployment. (source: www.meereisportal.de)

BROMEX, Eureka, SHEBA, N-ICE and GreenArc Campaigns. Further observational data on Arctic winter snow have also been collected from some field campaigns. SHEBA drifted in the Beaufort Gyre much like a Soviet NP station (1997-98). SHEBA data were collected with graded ski poles along snow lines similar (but shorter) to those of the Soviet stations (Sturm et al, 2002). The N-ICE field campaign north of Svalbard functioned similarly although it was forced to reenter the ice pack at times. Snow depth data was collected with a Magnaprobe (Merkouriadi et al, 2017). Finally the BROMEX campaign was conducted in March 2012 near Barrow, Alaska and was coincident with overflights. Depths were taken with Magnaprobe (Webster et al, 2014). The Danish GreenArc campaign was north of Greenland on fast ice in Spring 2009 as part of the international polar year. Measured depth every 5m on 2km transects (Farrell et al, 2012). The Eureka campaign was conducted in March-April 2014 on fast ice

near Nunavut, Canada. Between 26-29 March 37320 depth measurements were taken over a transect of 46km with 100m orthogonal transects and complementary OIB overflights (King et al, 2015)

5.2.3. Other snow datasets (WP2.3)

In addition to validating with airborne and in-situ data, we will compare our derived snow depths with other existing pan-Arctic snow depth products. As well as the two observation-based snow products summarised below, we will also compare against a suite of model-derived snow depth products, which are detailed in Table 7.

AMSR-E

The NASA AMSR-E instrument, a passive microwave radiometer aboard the AQUA satellite, launched in May 2002, uses the snow-depth-on-sea-ice algorithm to estimate both Arctic and Antarctic snow cover thickness from space (Comiso et al., 2003). The algorithm utilises the assumption that scattering increases with increasing snow depth, thus leading to a lower passive microwave brightness temperature. AMSR-E snow depth data are publicly available at: https://nsidc.org/data/AE_SI12/versions/3.

SMOS

The European Space Agency's Soil Moisture and Ocean Salinity (SMOS) satellite launched in 2009. Maaß et al. (2013) utilised SMOS's L-band frequency (1.4 GHz) to retrieve snow depth. Although snow is transparent to L-band frequencies, i.e. the large wavelengths are not attenuated by the snow, their model-based study found brightness temperatures from the ice increased at L-band frequencies when a snow layer was present due to its insulating properties and the dependence of ice emissivity on temperature. Although SMOS snow depths are not publicly available, the members of our consortium have access to the data via our project partner Lars Kaleshke at AWI.

Summary of snow products

Combined effort from several partners of this consortium has led to a collection and inter-comparison of most of the pan-Arctic snow products currently available. Zhou et al (in prep.) has listed these products in the Table 5 and we will use this preliminary work to assess the main differences between our newly developed product and this series of existing products from passive micro-wave (PMW Bremen, PMW DMI), reanalysis based snow products (SnowModel-LG, NESOSIM, CPOM, UW), and active satellite based products (DuST, DESS). Note that of these products DuST and CPOM were developed as part of the Arctic+ Snow project.

Product	Time span	Temporal resolution	Spatial resolution	Method type	Reference
SnowModel-LG	1980-2018	All year (daily)	25km×25km	Reanalysis-based	Liston et al (2019); Stroeve et al (2019)
NESOSIM	2000-2017	Aug to Apr (daily)	100km×100km	Reanalysis-based	Petty et al (2018)
CPOM	1991-2017	All year (daily)	10km×10km	Reanalysis-based	Tilling et al, in prep.

UW	1980-2015	Apr (monthly)	75km×75km	Reanalysis-based	Blanchard-Wrigglesworth (2018)
DuST	2003-2018	Bi-monthly (2013-2018) & monthly (2003-2008)	1.5° longitude × 0.5° latitude	Active satellite-based	Lawrence et al (2018)
DESS	2011-2019	Mar (monthly)	12.5km× 12.5km	Active & passive satellite-based	Xu et al (2019)
PMW Bremen	2003-2018	Mar & Apr (Daily)	25km×25km	Passive satellite-based	Rostosky et al (2018)
PMW DMI	2013-2018	Jan to Apr (monthly)	25km×25km	Passive satellite-based	Winstrup et al (2019)

Table 5- List of snow model products

5.3. Candidate test area

Candidate areas are meant to test prototype products with specific and known physical states of snow on sea ice. The general concept is inspired from the Arctic+ ice mass project, where ice thickness products were intercompared in three test areas for FYI, MYI and mixed ice types.

We follow this logic in this project and select candidate areas that are representative for the range of snow depths in the seasonal cycle. However, investigating snow depth requires a modification compared to the candidate test areas of the Arctic+ ice mass project. Snow on sea ice might melt completely during summer also in areas of perennial sea ice though the underlying sea ice layer might not. Thus, the distinction between thin and thick snow areas is not necessarily a function of the pre-dominant ice type but the period in the yearly cycle of accumulation and melt. Candidate areas on different ice types therefore serve the purpose to investigate snow accumulation on different surface types. This is especially important for snow products from dual-band altimetry that need to consider the combined impact of surface roughness and snow backscatter on the radar waveform shape. Similarly, the transition from cold dry snow to wet and then melting snow will be observed in all candidate areas. The candidate areas for snow on sea ice however need to meet the following crucial additional requirements that are now taken into consideration:

AltiKa orbit inclination: Snow depth products based on existing dual-band altimetry from both CryoSat-2 and AltiKa platforms are limited by the orbit inclination of AltiKa. The main candidate areas must therefore not exceed a latitude of 81.5 degrees north if they are to cover all available snow depth data sets.

Validation data: One of the objectives of the candidate test areas is to validate our products of snow depth on sea ice and thus requires the presence of ground truth by means of in-situ or airborne validation data. This criterion limits the usefulness of candidate test areas in the FYI regions of the Russian Arctic where little ground truth data exists. On the other hand, the existence of significant validation sets, such as the MOSAiC drift experiment, is a motivation for a candidate test area.

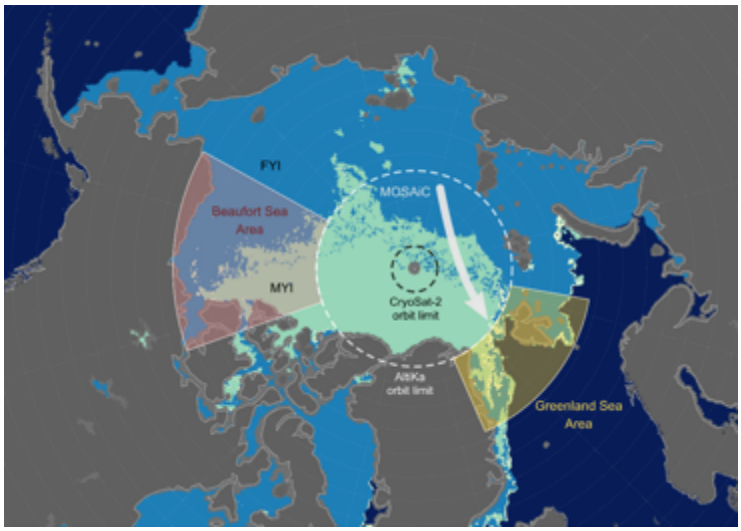

Figure 28: Map of test candidate sites in the northern hemisphere.

Not all candidate areas (Figure 28) can meet all requirements, we therefore define a set of areas that will serve different purposes, with a priority given to the presence of validation data. The main source of validation data are snow depth data sets from the NASA IceBridge and AWI IceBird airborne campaigns, which are limited to the Arctic and from snow buoys that are deployed in both hemispheres. Data from the snow buoy deployments in the Weddell Sea also give us the option to assess the skill of the challenging satellite retrieval of snow depth in the southern hemisphere.

The second priority is on the quality of the ground truth data. The MOSAiC expedition is providing an unprecedented level of information relevant for this project. Though the data collection will very likely be exclusively north of the AltiKa orbit inclination, the snow information collected during a full year is a primary validation data set for snow depth from combined radar (CryoSat-2) and laser (ICESat-2) altimetry. We therefore include MOSAiC as a Lagrangian candidate test area.

Area	Purpose	AltiKa coverage	Validation Data
Beaufort Sea	Evolution of snow depth on FYI and MYI in Arctic Winter season	Yes	NASA IceBridge AWI IceBird Snow buoys
Greenland Sea	Evolution of snow depth on FYI and MYI in Arctic Winter season	Yes	NASA IceBridge ESA CryoVEx AWI IceBird Snow buoys
MOSAiC (central Arctic)	Evolution of Ku/Ka radar backscatter properties, validation of CS2/IS2 snow depth	No	In-Situ snow depth, snow properties and KuKa backscatter
Weddell Sea	Year-around evolution of snow depth on sea ice in southern hemisphere	Yes	Snow buoys

Table 6 - Summary of key test areas chosen for validation of our snow products.

A by-product of our project and of our inverse modelling methods, will be to identify quantitatively regions that are poorly sampled and therefore where snow on sea ice has the largest uncertainty to make recommendations for future validation and calibration field and airborne campaigns.

6. SURVEY OF PAN-ARCTIC SNOW ON SEA ICE DATASETS

6.1. Summary of inputs, tasks and outputs

Inputs required to Start:
• SoW [EOP-SDR/SOW/087-17/DFP]
• Proposal [UCL-PRO-19-MT1]
Task Description:
• Review of historical products
• Review of snow on drifting sea ice products
• Review of passive microwave products
• Review of multi-frequency products
Outputs:
• Catalogue of available, appropriate datasets
• Contribution D1: Requirement Baseline (RB)

6.2. Historical products

The Warren Climatology. The Warren snow climatology ('W99') was assembled from data collected from Russian drifting stations ('NPs') from 1954-1991. Because only 29 stations (NPs 3-31) operated in this period, the climatology is assembled from a relatively small number of data points. It is very rare that the snow depth in a given year is measured by more than two stations. The dataset also has poor coverage in the Laptev and Kara seas, as well as south of 85N in the longitude range of -90 to 90 degrees. Furthermore, drifting stations were exclusively placed on multiyear ice. Snow depth was measured in two ways, in lines or at stakes. The line method consists of measurements at 10m intervals along 500m lines, although in 1/3 of cases the lines were 1000m long. Line orientation was randomly chosen at the founding of the station. The climatology is preferentially developed from snow line measurements as they're more isolated from activities around the station and offer better sampling of the snow depth distribution.

Modified Warren (mW99). Based on Operation Ice Bridge flights from April 2009 (Kurtz and Farrell, 2011), Laxon et al. (2013) elected to halve W99 snow depths over first year ice. Analysis of further OIB flights tends to support this method, as explored by Webster et al. (2014). However, OIB flights preferentially sample the North American side of the Arctic (North of Greenland and Beaufort Gyre), which introduces significant uncertainty into the halving regime of mW99.

Modified Warren merged with AMSR2. The original regional scope of the Warren snow climatology is limited to the central Arctic basin. The climatology itself is expressed as a two-dimensional quadratic fit that is prone to yield unphysical values for both snow depth and density if evaluated in regions outside the central Arctic Ocean, e.g. the Barents Sea or in Baffin Bay. To mitigate this issue and improve accuracy of freeboard and thickness estimates, Hendricks and Ricker (2020) proposed a snow

depth climatology that is based on W99 in the central Arctic Basin and the AMSR2-based snow depth climatology over FYI from the University Bremen in all other regions. W99 and AMSR2 data are merged by a static regional weight function and the W99 modification (mW99) is maintained though it is not applied to the AMSR2 snow climatology.

W99 + Sever. As well as putting out drifting stations, the Soviet Union/ Russia also carried out a significant airborne campaign ('Sever') in the spring months. The Shalina and Sandven (2019) ('SS') climatology is synthesised from snow observations during 1959-86 in March, April and May. The SS climatology for these months is dominated by Sever measurements rather than those from drifting stations (94% vs 6%). The Sever data sampling is highly biased towards the Russian side of the Arctic in the shelf seas, and like W99 does not extend through the Fram Strait or into the Barents Sea. The majority of data in the climatology also comes from the 1970s. Data from the '60s and '80s is largely confined to the Siberian shelf seas and does not include the Central Arctic region. While more limited in its seasonal nature, Sever data includes a much more comprehensive set of snow variables on features such as hummocks and sastrugi. Furthermore, data is available for FYI as well as MYI.

6.3. Snow on drifting sea ice products

An alternative approach to solely satellite derived snow products is illustrated with the mixed model-observations products combining model representation of snow accumulation on satellite derived sea ice drifting parcels. Several of these models are produced by members of our consortium and while they will not represent the core development of our project they will be accompanying our algorithmic developments for comparison and snow on sea ice process understanding.

CPOM snow on drifting sea ice product

This product was developed in collaboration with the Arctic+ Snow project. The CPOM snow depth product (Tilling et al, in prep) is initialized on a Lagrangian grid with a spacing of 10 km running from 40°N to the pole and steps daily through the winter, accumulating snow-water-equivalent (SWE) of snow from reanalysis forcings and advected along sea ice drift trajectories provided by the NSIDC Polar Pathfinder ice motion dataset. A fraction of the accumulated snow is removed when the wind speed exceeds 5ms^{-1} using a function proportional to wind speed and lead fraction in (Schroeder et al, 2019, table 1). Finally, the total column of accumulated SWE at each Lagrangian point is converted to snow depth using a daily snow density function constructed in a similar (but not identical) way to Kwok and Cunningham, (2008), which is added to the initial snow layer (if present). The irregularly spaced snow data from the Lagrangian grid are re-gridded onto a regular 10 km^2 Polar stereographic projection using an averaging radius of 50 km to give both a snow depth map and a snow load map for each day of winter. The temporal resolution of SnowModel is daily between August 1980 to present.

SNOWMODEL

SnowModel is also used in a Lagrangian framework to redistribute snow around the Arctic basin as ice moves. Physical snow processes are included, such as blowing snow redistribution and sublimation, density evolution and snow pack metamorphosis. Tracking begins on 1st August in 1980 assuming snow-free initial condition, and accumulates snow until 31 July the next year. On 31 July, any remaining snow that becomes isothermal and saturated with meltwater becomes superimposed ice and is no longer identified as 'snow'. This is the only data product that includes snow depth during the melt

season. Weekly ice motion vectors are linearly interpolated to daily resolution. Output includes snow depth, snowfall amount, rainfall amount, snow water equivalent (SWE) and snow density (Stroeve et al, 2019), and are provided on a 25km x 25km EASE grid. The temporal resolution of SnowModel is daily between August 1980 to present.

NESOSIM

The NASA Eulerian Snow On Sea Ice Model (NESOSIM) is a three-dimensional, two-layer (vertical), Eulerian snow budget model (Petty et al, 2018). NESOSIM includes two snow layers: old compacted snow and new fresh snow. Wind-packing and snow loss to the leads are included, though these are not constrained by observations. Instead, those were implemented in order to tune the model to match the observed/historical seasonal cycles in snow depth and density. NESOSIM was run using several atmospheric reanalyses, NSIDC sea ice drift vectors and Bootstrap ice concentrations. Model calibrations (i.e. tuning of snow loss into leads) are carried out with Soviet drifting data as ground truth. Snow accumulation is initialized at the end of summer (default of August 15th) and run until the following spring (May 1st). Snow depth is equally divided into the 'old' and 'new' snow layers, with snow transferred from the 'new' to the 'old' snow layer based on the wind conditions. Snow is then accumulated and evolves dynamically with sea ice motion through a divergence–convergence and an advection term. Daily snow depth (mean depth only over sea ice), snow density and snow volume (per unit grid-cell) are available from August 15th to April 30th for each year, at a spatial resolution of 100km × 100km in a polar stereographic grid, and from 1980 to present.

SNOWPACK + SMRT. Sea ice and overlying snow thickness are currently estimated via satellite remote sensing using radar altimeters and microwave radiometers respectively. However, retrievals of these quantities are influenced by the snowpack stratigraphy (Figure 29, Radar: e.g. Willatt et al, 2011; King et al, 2018), (Radiometry: e.g. Comiso et al, 2003; Fuller et al, 2015). To improve these estimates, the stratigraphy of the snowpack at the time and place of remote sensing is estimated through analysis of its historical meteorological exposure. This is achieved through the advection of tens of thousands of "virtual ice parcels" around the Arctic basin during a winter season using ice motion vectors. Information on the overlying snow will be gained through running a recently published snow accumulation model (SNOWPACK Sea Ice Module v1.0; Wever et al, 2020) on the track of each virtual ice parcel. This has already been achieved for a trial group of ice parcels and has produced stratigraphies with large-grained, highly scattering layers.

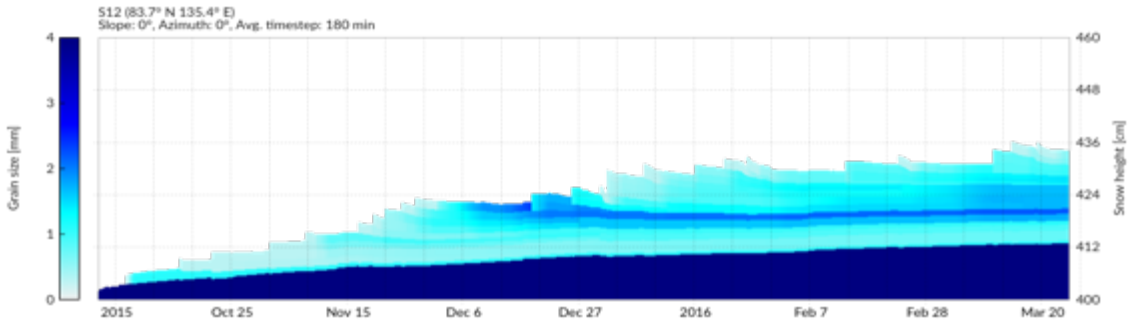

Figure 29- SNOWPACK model output illustrating the development of a layered snowpack over the 2015-16 winter. A warm event in early December led to a layer of enlarged, rounded grains; this layer was then buried by later snowfall but continued to act as a strong scattering horizon. Credit: Robbie Mallett (UCL).

The simulated overlying snowpack will then act as the input to a microwave radiative transfer model

(SMRT; Picard et al, 2018) and the effects of its stratigraphy on its microwave emission signature will be estimated. It is planned that the modelled effect of stratigraphy on emissions will be used to correct snow depth estimates based on microwave radiometry. It is also anticipated that an "altimetry mode" will be released for SMRT, allowing the modelling of a radar scattering horizon in a snowpack. This calculation is not possible as it stands due to the nature of SMRT's numerical solver (The Discrete Ordinate and Eigenvalue Solver; Stamnes et al, 1988; Picard et al, 2013). Successful modelling the snowpack's stratigraphy on a Pan-Arctic scale would deliver insight into suitable interpretation of active and passive microwave remote sensing as well as radar altimetry.

CICE sea ice and snow climate model

CICE is a dynamic thermodynamic sea ice model developed at Los Alamos (with collaboration from CPOM) and designed for inclusion within a global climate model. LIM is a similar model developed in Belgium. The advantages of using this type of sophisticated sea ice models for this study is that it provides a realistic and physically constrained boundary for the snow cover accounting for interactions of the sea ice and snow with the underlying ocean. CICE and LIM are coupled with the ocean model NEMO and those coupled version were used extensively as part of the Arctic+ project respectively at CPOM (UoR) and University of Helsinki. For a more detailed description of these model see our model papers (Schroeder et al, 2019; Uotila et al, 2017).

6.4. Passive microwave products

Kern & Ozsoy (2019) provide a good review of recent developments in passive microwave approaches for remote sensing snow thickness retrievals on sea ice. At its core the technique (Rostosky et al., 2018) relies on the fact that top of the snow brightness temperature is reduced as (i) volume scattering increases with decreasing wavelengths towards the typical size of snow grains (~1-3mm) and (ii) as the snow deepens and therefore more volume scattering ensues. Additional filtering out of wet snow surfaces is also needed as even a small liquid content in the snow will strongly affect the wave scattering (Ulaby & Long, 2014, pp. 593–594).

Empirical Snow thickness formula	Ice type	Reference
$Hs = 2.9 - 782 \cdot \frac{Tb^*_{37} - Tb^*_{19}}{Tb^*_{37} + Tb^*_{19}}$	FYI / MYI*	Comiso et al (2003)
$Hs = 19.74 - 556.69 \cdot \frac{Tb^*_{19} - Tb^*_{7}}{Tb^*_{19} + Tb^*_{7}}$	FYI	Rostosky et al (2018)
$Hs = 18.73 - 376.32 \cdot \frac{Tb^*_{19} - Tb^*_{7}}{Tb^*_{19} + Tb^*_{7}}$	MYI	
$Hs = 177 - 1.75 \cdot Tb_7 - 2.80 \cdot Tb_{19} - 0.41 \cdot Tb_{37}$	FYI / MYI	Killic et al (2019)
$Hs = NN\left(GR\left(\frac{37}{19}\right), GR\left(\frac{37}{19}\right), \quad PR(37)\right)$	FYI/MYI	Braakmann-Folgmann and Donlon (2019)
$Hs = NN\left(GR\left(\frac{37}{19}\right), GR\left(\frac{37}{19}\right), PR(37), PR(1.4)\right)$	FYI/MYI	

Table 8 – Empirical formulations for snow thickness as a function of brightness temperatures from passive microwave radiometers. Tb^* is the corrected brightness temperature for the ice covered part of the footprint while Tb refers to the ice brightness temperature. MYI* signals that in the original paper the snow was not calculated over MYI.

The method was first developed for Antarctic sea ice applications (Markus et al (1998; 2006)) at the frequencies of 19.35 GHz and above observed by satellite SSM/I (Special Sensor Microwave/Imager). The authors used a linear regression between the gradient ratio, $GR(37/19)$, of the vertically polarized brightness temperature observations at 19 and 37 GHz and Antarctic snow depth measurements. The same authors (Comiso et al, 2013) adapted this technique (see Table 8) to the latest passive microwave satellites (Advanced Microwave Scanning Radiometer for EOS (AMSR-E) and, since 2012, AMSR2) and implemented it for Arctic first year ice (FYI) snow thickness retrievals of up to 50 cm thickness (Cavalieri et al., 2012) with the following empirical expression for the gradient ratio as a function of snow and open water brightness temperatures and sea ice concentration:

$$GR(37/19) = \frac{Tb_{37} - Tb_{19} - (Tb_{37,\ ow} - Tb_{19,\ ow})(1 - C)}{Tb_{37} + Tb_{19} - (Tb_{37,\ ow} + Tb_{19,\ ow})(1 - C)}$$

Different frequencies respond differently to different surface snow characteristics with lower frequencies being less sensitive to the vertical structure on the snow pack (depth hoar, weather effects, ice layers, etc) but more sensitive to large scale roughness (i.e. snow and ice topography, ridges, sastrugi etc). Brucker and Markus (2013) re-assessed this empirical Arctic model and found that it needed re-calibrating possibly due to the changing nature of the snow surface and ice type repartition between FYI and MYI.

In a recent study, Rostosky et al, (2018), combined all these ideas and proposed an updated passive microwave snow thickness model with new regression coefficients (see Table 1) taking advantage of the fact that AMSR-E and AMSR-2 also operate at lower frequencies (both instruments work at 6.9 and 10.7 GHz and AMSR-2 also has a 7.3 GHz channel). Rostosky et al (2018) compared the skill of several gradient ratios against OIB snow thickness data over both FYI and MYI and found $GR(19/7)$ to be the optimal compromise over both ice type (respectively with a correlation of R=-0.73 and RMSD=4.3cm, see their Table 1).

Kilic et al (2019) built on the work of Rostosky and extended the approach to the full winter season using a two-step multi-linear regression approach with in addition to OIB snow depth data, calibration from Ice Mass Balance (IMB) buoys. An optimal empirical linear regression of snow depth vs brightness temperatures for this model is provided as shown in Table 8 As discussed in Stroeve et al., (2005), these passive microwave empirical methods for snow thickness calculation remain sensitive to snowpack conditions and surface roughness.

Maaß et al (2013) demonstrated that it was possible to retrieve snow thickness of up to 35 cm over sea ice thicker than 1-1.5 m by using the even lower 1.4 GHz frequency (L-band) measured by ESA's Soil Moisture and Ocean Salinity (SMOS) satellite. Note that the snow is transparent to this frequency as it does not attenuate those larger wavelengths but instead the snow layer indirectly modulates the brightness temperature from the ice due to its insulating properties and the dependence of ice emissivity on temperature. The authors acknowledge that their results are sensitive to the input parameters of their model (i.e. ice temperature, thickness, salinity and snow density) and that the method requires further calibration and development. Currently, no SMOS derived snow product has been made publicly available.

Finally, Braakmann-Folgmann and Donlon (2019) intercompare these methodologies and propose a generalised approach to represent any possible functional dependence between snow thickness and a selection of relevant inputs within a neural network (NN) framework. First, they propose a AMSR2 only model relying on three inputs, namely $GR(37/19)$, $GR(19/7)$, and the polarized ratio $PR(37)$ between vertically and horizontally polarized brightness temperatures:

$$PR(37) = \frac{Tb^*_{37,V} - Tb^*_{37,H}}{Tb^*_{37,V} + Tb^*_{37,H}}$$

where Tb^* denotes the corrected brightness temperature for the ice-covered part only of the footprint while Tb refers to the ice brightness temperature. The authors propose a second neural network model accounting also for the polarized ratio at the SMOS L-band frequency $PR(1.4)$. Figure 7 below shows the distributions of snow thicknesses retrieved by the various algorithms and compares them with the airborne derived snow thicknesses from Operation IceBridge (OIB). The best performing models appear to be the generalized NN models with AMSR2 only and with AMSR2+SMOS data.

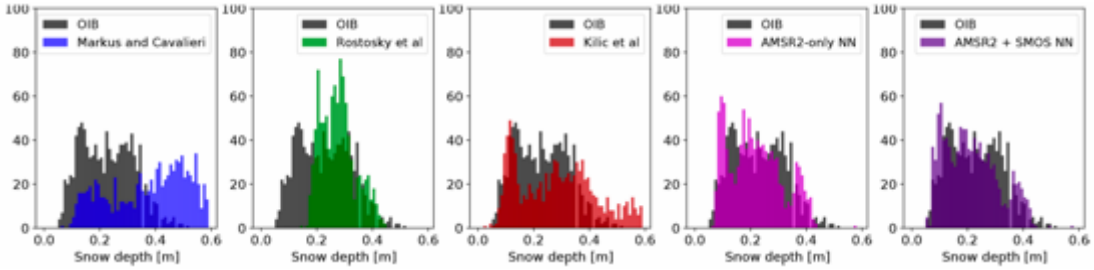

Figure 30 - Distribution of OIB-measured snow depth (all data) in grey versus estimated snow depth using different algorithms in colour (Braakmann-Folgmann and Donlon, 2019).

Passive microwave methods show promise but in addition to the limitation of the empirical methods listed above they also suffer from an important reduction of spatial resolution with decreasing frequency (i.e. AMSR2 has a 35 km × 62 km footprint at 6.9 GHz). To overcome this the European Space Agency (ESA) is preparing a High Priority Candidate Mission (HPCM) called the Copernicus Imaging Microwave Radiometer (CIMR; Donlon and CIMR Mission Advisory Group, 2019) that will operate jointly at a wide range of frequencies and increased spatial resolutions, respectively 1.4 GHz (60 km), 6.9 and 10.65 GHz (< 15 km), 18.7 GHz (5–6 km), and 36.5 GHz (4–5 km)).

We now review the recent approaches to retrieve snow thickness relying on multi-frequency altimetry that will constitute the heart of this project.

6.5. Multi-frequency altimetry products

Table 9- Past and present altimeter missions

	Envisat (RA2)	AltiKa (SARAL)	CS2 (SIRAL)	Sentinel 3A/B (SRAL)	ICESat (GLAS)	ICESat-2
Orbital inclination	98.5°	98.5°	92°	98.65°	94°	92°

Operational period	2002-2012	2013-present	2010-present	S3A:Feb 2016 - present S3B: Apr 2018 - present	2003 -2008	Sept 2018 – present
Repeat cycle	35 days until 10/2010 then allowed to drift	35 days	369 days; 30 day sub cycle	27 days	8 days (until 10/2003) 91 days (33 days sub-cycle) 10/2003 onwards	91 days exact repeat
Centre frequency	13.575 GHz	35.75 GHz	13.575 GHz	Dual 13.575 GHz / 5.41 GHz	532 nm laser	532 nm laser
Beamwidth	1.3°	0.6°	1.3°	1.3°	<0.001°	<0.001°
Bandwidth	320 MHz	500 MHz	320 MHz	320 MHz	N/A	N/A
Range resolution in free space	47 cm	30 cm	47 cm	47 cm	N/A	N/A
Footprint	1.7 km pulse-limited; 1.8 km beam-limited	1.4 km pulse-limited; 8 km beam-limited	~380 m along track; 1.7 km pulse-limited across track	~380 m along track; 1.7 km pulse-limited across track	70m	17 m

Over the past two decades both radar (e.g. ERS-1/2, Envisat, CryoSat-2, AltiKa) and laser (e.g. ICESat, ICESat-2) altimeters have enabled sea ice thickness to be measured from space (Laxon et al., 2003, 2013; Kwok and Cunningham, 2008). The first step of this retrieval consists in measuring the distance from the satellite to a dominant scattering horizon within the snow pack – with the so-called *radar freeboard* shown in Figure 31 the elevation of the scattering horizon above the local sea surface.

Traditionally, radar altimeters have operated at a Ku-band frequency (~13.6 GHz) with the assumption that the dominant scattering horizon is the snow-ice interface and therefore that the radar freeboard can be identified to the (real) *sea ice freeboard* (once a correction factor for the delayed wave propagation into the snow pack is accounted for). For laser altimeters, photons are overwhelmingly reflected at the air-snow interface and the *laser freeboard* can be identified to the *sea ice and snow freeboard*. The radar altimeter AlitKa operates at a Ka-band frequency (~35 GHz) that is 55 more sensitive to volume scattering from the snow layer (Remy et al, 1999) with the dominant scattering somewhere within the snow pack and likely closer to the air-snow interface. It is our main goal is this project to exploit these differences in penetration into the snow pack and develop a multi-frequency altimetry approach to retrieve snow thickness and other characteristics.

Figure 31: Illustration of the terms laser (snow) freeboard, F_l, the sea ice freeboard, F_i, the radar freeboard, F_r and snow depth, d. The horizontal dashed red line is the dominant scattering horizon.

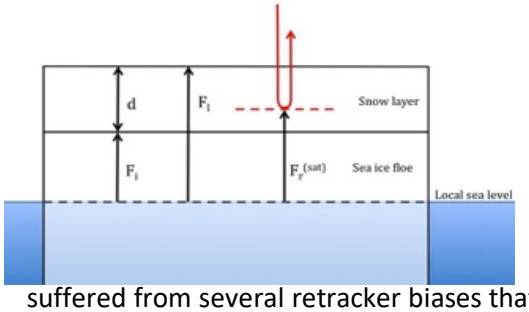

Armitage and Ridout (2015) and Maheshwari et al (2015) were the first to estimate the radar freeboard from the Ka-band altimeter AltiKa and found different penetration factors in the snow with less than 50% penetration for the former and total penetration of the snow pack for the latter. Armitage and Ridout (2015) compared the radar freeboard and found that AltiKa generally retrieves a higher elevation over sea ice when compared with radar freeboard from CS2. While these early results may have suffered from several retracker biases that we will address in detail in our project, they nevertheless opened the door to several follow up studies proposing to estimate snow thickness from coincident satellite radar altimeters operating at different frequencies.

Bias correction methodology. Assuming zero penetration depth into the snow for AltiKa and total penetration for CryoSat-2, Guerreiro et al (2016) were able to produce a snow thickness product as the difference of these two elevation retrievals. To minimize satellite footprint dependence of the elevation retrievals the authors used a Pseudo Low Resolution Mode (PLRM) provided by CNES for CryoSat-2 to mimic the conventional Low Resolution Mode (LRM) of AltiKa and remove any bias due to the footprint shape. As shown in Figure 32, the resulting snow maps were shown to correlate well with ice thickness types with thicker snow overlapping with older multi-year ice (MYI). Comparison with OIB snow thickness showed good agreement with a RMSE of the order of 5cm with a thinner ice cover over the period analysed (2013-2015) than the Warren climatology (representative of the 1954-1991 period).

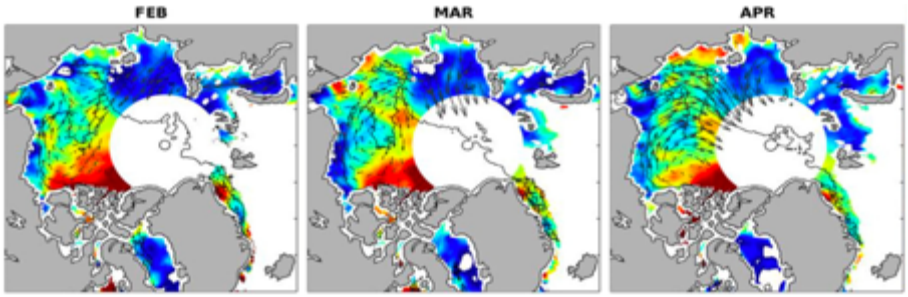

Figure 32 – Spatial monthly maps of snow depths for November 2013 to April 2014. The black solid line shows the position of MYI edge from OSI SAF. The corresponding OSI SAF monthly sea ice drift is also shown (black arrows).

Calibration methodology. Lawrence et al (2018) took a similar approach but relaxed the condition of a zero penetration for AltiKa and used instead a calibration approach with OIB airborne data whereby the radar freeboard from AltiKa is aligned with the snow surface and the radar freeboard from CS2 to the snow-ice interface. Each calibration curve accounts for spatial variability via a dependence on the surface roughness parameterized by the pulse peakiness for each satellite. Snow depth is then found as the difference between the two calibrated freeboards, with a correction added for the slower speed of light propagation through snow (Figure 33). The authors found comparable RMSE of ~5-7 cm for their snow product against independent OIB snow thickness estimates.

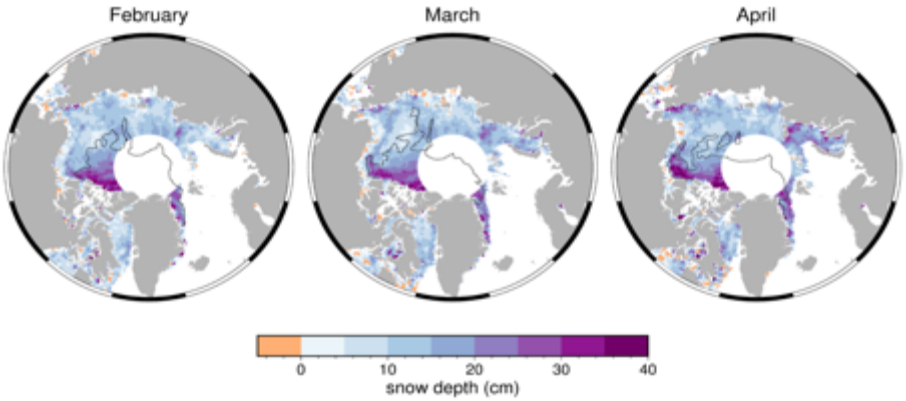

Figure 33 – Monthly snow depths for the growth season November 2015 to April 2016. The multi-year boundary for each month is shown by the dashed black line adapted from the OSI SAF product.

The same authors further demonstrated the applicability of this type of calibration methodology to ICESat and Envisat by adjusting the Envisat radar freeboard to the 'true' operation ice bridge ice-snow interface and assuming a scattering horizon from the top of snow for ICESat. Figure 33 (WP3) shows the corresponding calibration curve as a function of the Envisat pulse peakiness and the corresponding snow thickness map for February/March 2006. With the successful launch of ICESat-2 in 2018, this type of methodology can now be extended (see WP3) to combine effectively radar and laser altimetry from CryoSat-2 and ICESat-2 data to derive novel snow thickness products.

As a final example of a multi-satellite snow product involving altimetry, Xu et al (2017) (Project partners SX and LZ) proposed to combine passive L-band microwave from SMOS with active remote sensing from laser altimeters as a way to retrieve jointly sea ice and snow thickness information. Zhou et al (2018) inverted for the forward equations of (i) the L-band radiative model,

$$Tb = Tb\big(Hs, Hi, Tsfc, ice\_type, Tw, Sw\big)$$

(ii) the altimetry isostatic model for laser

$$Hi = \frac{\rho_W}{\rho_w - \rho_i} \cdot Fi + \frac{\rho_s}{\rho_w - \rho_i} \cdot Hs$$

together with (iii) an empirical co-variability equation derived from OIB data between snow depth and total snow and radar freeboard

$$Hs = \alpha \cdot (\beta \cdot Fl)$$

As shown in Figure 34, these equations can be inverted for numerically and the three unknown variables, Hs, Fl, and Hi recovered. Note that this methodology could be adapted to use also the radar isostatic model

$$Hi = \frac{\rho_W}{\rho_w - \rho_i} \cdot Fl - \frac{\rho_w - \rho_s}{\rho_w - \rho_i} \cdot Hs$$

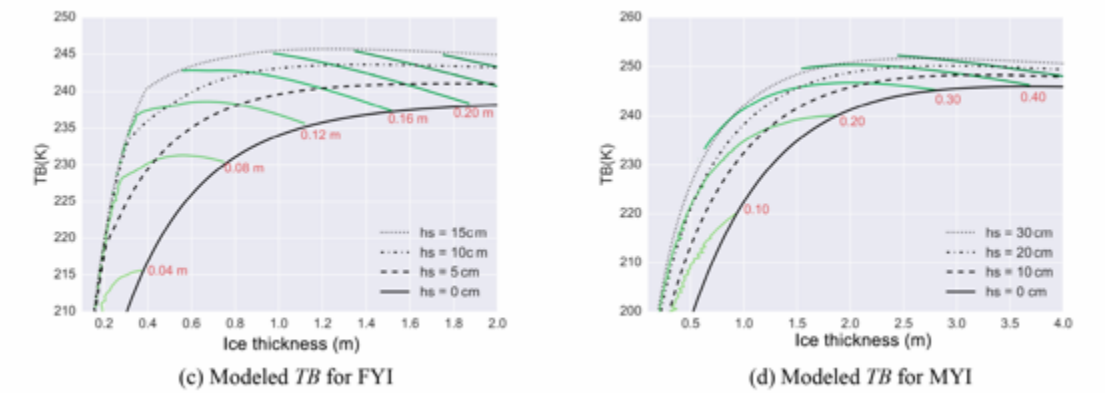

Figure 34 - Panels (c) and (d) show the modeled TB under typical sea ice parameters (hi and hs), assuming Arctic winter conditions (surface temperature of −30 ◦C). The green lines represent constant snow freeboard lines. Constant FBsnow lines and corresponding values (in green) of FBsnow are in red.

7. PRESENT AND FUTURE INITIATIVES

7.1. Summary of inputs, tasks and outputs

Inputs required to Start:
• SoW [EOP-SDR/SOW/087-17/DFP]
• Proposal [UCL-PRO-19-MT1]
Task Description:
• Review gaps and initiatives in sea ice thickness processing chains
• Identify recent initiatives
• Identify opportunities for future polar altimetry missions
Outputs:
• Contribution D1: Requirement Baseline (RB)

7.2. Snow for satellite sea ice thickness retrievals

The Arctic+ Snow project had already outlined international initiatives that are concerned with the improvement of snow information on sea ice such as:

- the Canadian Sea Ice and Snow Evolution (CanSISE) Network
- Environment Canada's and the Canadian Space Agency's Snow Mission initiative
- NASA SnowEX and iSWGR initiatives
- the IACS MicroSnow working group
- NASA's Snow Thickness on Sea Ice Working Group (STOSIWIG)
- ESA's CryoSat validation experiments (CryoVEx).

While most of those initiatives are still active, our results will contribute to informing them and to help them direct their research and activities into the best possible direction. In most cases, the initiatives are concerned with the provision of better observations and validation data, and therefore the results of our impact assessment are particularly important to define mission requirements and other quality criteria.

On the modelling side too, efforts are underway to assess the role of the snow cover on sea ice model. Using the same model that was used to perform the impact assessment of the new snow products, Stroeve et al (2017) and Schroeder et al., (2018) showed that variations in snow characteristics (thickness, spatial distribution, inter-annual variability, etc…) could play a leading order role in the evolution of the total volume of sea ice over the growth season (i.e. October to April). These approaches open the door to more in depth use of the snow products developed in this project in the framework of operational data assimilation activities (for example in partnership with CMEMS, ECMWF) and as part of international forecasting efforts (SIPN, YOPP).

In a broader sense, our results will inform snow related activities of the World Climate Research Programme's Climate and Cryosphere (CliC) program, and the international sea ice prediction network where observations and modelling of snow are advanced.

7.3. Recent snow on sea ice developments

From the time of writing of the proposal several studies have emerged from different groups internationally. We note as of particular importance some recent developments in our understand of the radar snow interactions thanks to the efforts of the MOSAiC project and more specifically the KuKa instrument deployed by the UCL / Manitoba team led by Julienne Stroeve (Stroeve et al, 2020).

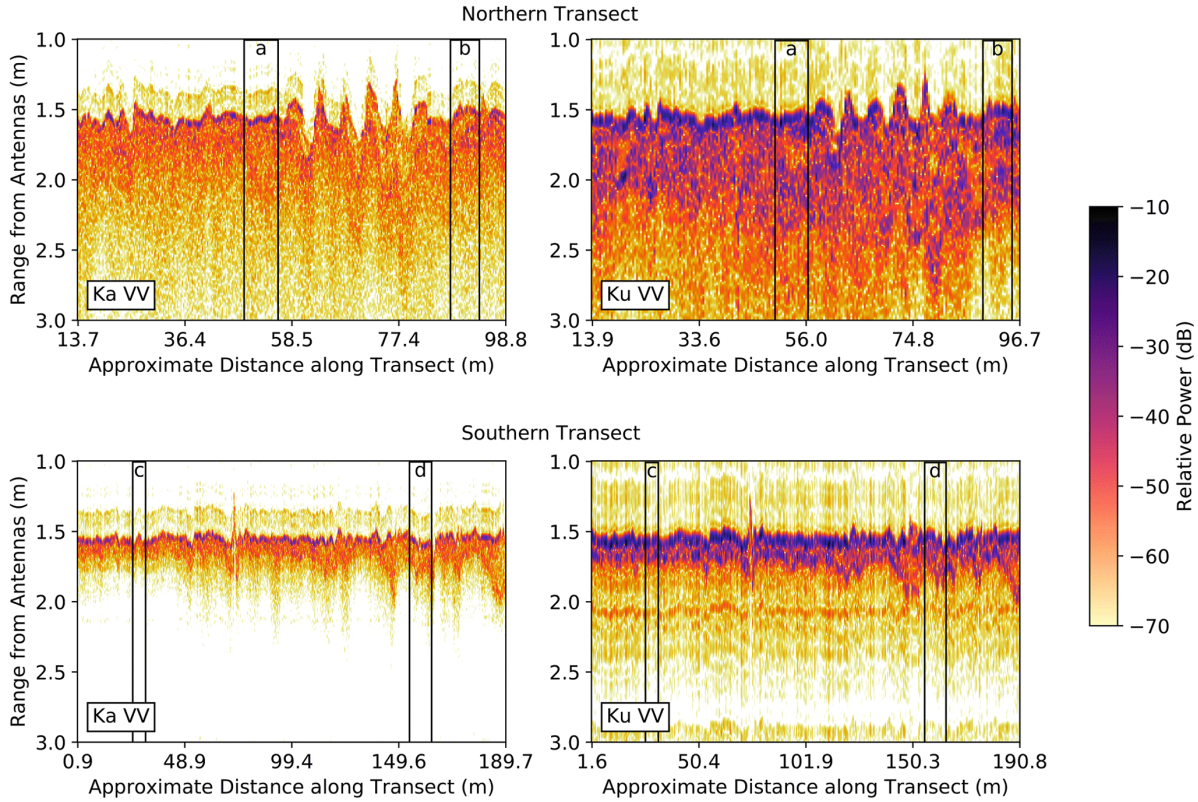

Figure 35 - Ka- (left) and Ku- (right) band VV-polarized power as a function of distance along the northern (top) and southern (bottom) transect. Data acquired on 16 January 2020 at 10:52 and 12:02 UTC for the northern and southern transects, respectively. Letters a–d denote four sections shown in more detail in Fig. 8, each 6 m wide (corresponding to 6 m of travel along the transect). Data are not evenly spaced along the x axis; tick marks indicate distances along the transect where the samples were obtained (Stroeve et al, 2020).

Our NASA partners have also made progress in developing the multi-frequency approach combining laser and rader altimetry (Kwok et al, 2021). In this first analysis the authors combined laser and radar freeboard to deduce a snow thickness assuming that the dominant scattering for Ku-band radar freeboards comes from the snow-ice interface. With this assumption Kwok et al (2019) produced snow maps that were compared with snow depth accumulated drifting Lagrangian sea ice from reanalysis (ERA-5 and ERA-I, Figure 34).

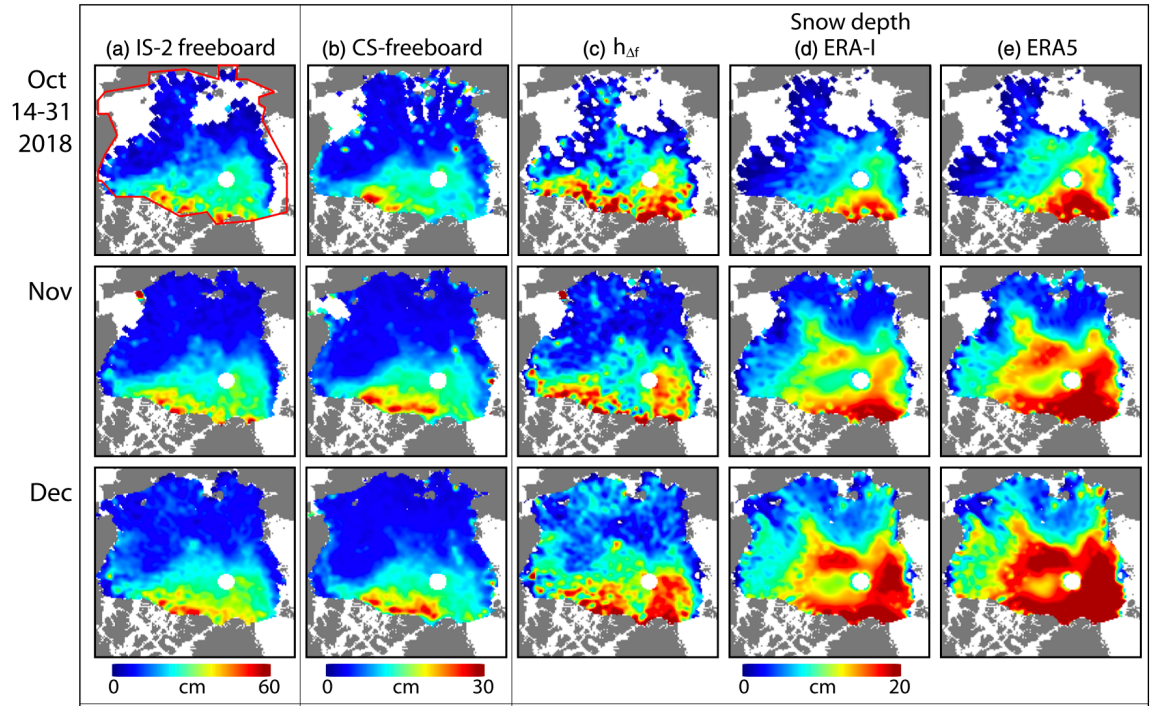

Figure 36 - Monthly composites of (a) IS-2 freeboard, (b) CS-2 freeboard, (c) retrieved snow depth ($h_{\Delta f}$) and snow depth reconstructions using (d) ERA-Interim and (e) ERA5 reanalysis products for the period between October 2018 and April 2019. Boundaries of the Arctic Ocean are shown in the top left panel (red). Figure and caption from Kwok et al (2020).

These two examples demonstrate the importance for our research to be developed with a constant dialogue with the scientific community about the validity and usefulness of the products generated. Community networks such as 'Cryolist' will be used as a tool for contacting the scientific community alongside targeted emails to key specialists, many of whom the consortium members already have professional working relationships with. Recommendations for future development of these products will be requested. Following this consultation, a scientific plan will be developed for improving the accuracy of the prototype products and a strategy for incorporating the products into existing initiatives will be detailed.

7.4. Paving the way to operational altimetry

7.4.1. Expected performance of CRISTAL candidate mission

At present there are only few satellite sensors in operation that are suitable for the retrieval of snow depth on sea ice. These are passive microwave sensors and altimeters at different observation frequencies. Therefore, the extent to which new methods can be developed is somewhat limited. The most promising current possibility lies with the combination of ICESat-2 laser altimeter and other missions' radar altimeter sensors.

While CryoSat-2 is the obvious candidate due to its similar orbit, only the Sentinel-3 constellation guarantees operational continuity but not at high latitudes. In this regard it is particularly important to assure the continuation of altimetry missions, for example a high inclination radar altimetry mission

such as the altimeter of the potential Copernicus Polar Ice and Snow Topography Altimeter (CRISTAL). The planned dual-band capability also brings the prospect of observing freeboard and snow depth from the same platform, which would provide an operational data source and reduce the uncertainty from imperfect colocation of two altimeter mission with different orbit configurations over drifting sea ice. For the retrieval of snow information of sea ice there is significant synergy between CRISTAL and the Copernicus Microwave Imaging Radiometer (CIMR), allowing data fusion of two different approaches to measures snow depth on sea ice.

7.4.2. Expected performance of CRISTAL candidate mission

Operational use of snow thickness information is at its infancy. Operational centres are mostly interested in ice thickness. As even ice thickness model and observation products have high uncertainties the improvement of snow information is a secondary problem at the moment. Nonetheless snow on sea ice has direct implications for example to winter navigation – as a rule of thumb mariners usually add the snow thickness to ice thickness when assessing friction between snow covered sea ice and a ship breaking it. In special circumstances (dense, thick and dry snow) snow friction can be even larger than that of ice.

However, as the generation of CryoSat-2 ice thickness products has reached some level of operational maturity and is part of e.g. the Copernicus Marine Services portfolio, operational, near-real-time snow thickness products could lead to an instantaneous improvement of the CryoSat-2 thickness products. The same will be most important for the ICESat-2 ice thickness data generation. However, near-real-time, operational use of snow thickness products will require that their uncertainties are low and quantified. This goal could be reached through the continued improvement of the products outlined in WP3 and WP4.

At the same time, operational reanalysis centres like NCEP and ECMWF could use better snow products to constrain their precipitation and snow-redistribution approaches, and to improve the thermodynamics at the ice-air interface. As reanalysis products are not generally generated in near-real-time this becomes much more feasible at it leaves sufficient time for the calibration and validation of the snow products.

The snow project shall also be tested in the FMI operational Kara sea forecast model, based on NEMO-LIM engine, providing IMO Polar Code compliant POLARIS Risk Index Outcome values for different ship classes in the Kara sea region (see http://ice.fmi.fi/data/kara-sea/sea-ice-forecasts_kara/). As the prototype product is not a NRT service, we shall assess its impact on historical runs - nudging the initial conditions from original snow model values to the prototype product ones and assessing the effect this has on the RIO values in the 2 weeks forecast.

8. REFERENCES

Armitage, T.W. and Ridout, A.L. (2015). Arctic sea ice freeboard from AltiKa and comparison with CryoSat-2 and Operation IceBridge. *Geophysical Research Letters*, 42(16), pp.6724-6731.

Blanchard-Wrigglesworth, E., & Bitz, C. M. (2014). Characteristics of Arctic sea-ice thickness variability in GCMs. *Journal of Climate*, *27*(21), 8244-8258.

Blazey, B. A., Holland, M. M., & Hunke, E. C. (2013). Arctic Ocean sea ice snow depth evaluation and bias sensitivity in CCSM. *The Cryosphere*, *7*(6), 1887-1900.

Bodin, T. and Sambridge, M., 2009. Seismic tomography with the reversible jump algorithm. *Geophysical Journal International*, *178*(3), pp.1411-1436.

Braakmann-Folgmann, A. and Donlon, C. (2019). Estimating snow depth on Arctic sea ice using satellite microwave radiometry and a neural network. *The Cryosphere*, *13*(9), pp.2421-2438.

Bronner, E., Guillot, A., & Picot, N. (2016). SARAL. *AltiKa Products Handbook*, 1-76

Brucker, L., & Markus, T. (2013). Arctic-scale assessment of satellite passive microwave-derived snow depth on sea ice using Operation IceBridge airborne data. *Journal of Geophysical Research: Oceans*, *118*(6), 2892-2905.

Cavalieri, D. J., Parkinson, C. L., Gloersen, P., & Zwally, H. J. (1996). Sea Ice Concentrations from Nimbus-7 SMMR and DMSP SSM/I-SSMIS Passive Microwave Data, Version 1.

Cavalieri, D. J., T. Markus, and J. C. Comiso. (2014). AMSR-E/Aqua Daily L3 12.5 km Brightness Temperature, Sea Ice Concentration, & Snow Depth Polar Grids, Version 3. Boulder, Colorado USA. *NASA National Snow and Ice Data Center Distributed Active Archive Center*. doi: https://doi.org/10.5067/AMSR-E/AE_SI12.003.

Comiso, J. C., Cavalieri, D. J., & Markus, T. (2003). Sea ice concentration, ice temperature, and snow depth using AMSR-E data. *IEEE Transactions on Geoscience and Remote Sensing*, 41, 243–252.

Connor, L.N., Laxon, S.W., Ridout, A.L., Krabill, W.B. and McAdoo, D.C., 2009. Comparison of Envisat radar and airborne laser altimeter measurements over Arctic sea ice. *Remote Sensing of Environment*, *113*(3), pp.563-570.

Farrell, S.L., Kurtz, N., Connor, L.N., Elder, B.C., Leuschen, C., Markus, T., McAdoo, D.C., Panzer, B., Richter-Menge, J. and Sonntag, J.G. (2011). A first assessment of IceBridge snow and ice thickness data over Arctic sea ice. *IEEE Transactions on Geoscience and Remote Sensing*, *50*(6), pp.2098-2111.

Fuller, M. C., Derksen, C., & Yackel, J. (2015). Plot scale passive microwave measurements and modeling of layered snow using the multi-layered HUT model. *Canadian Journal of Remote Sensing*, *41*(3), 219-231.

Giles, K. A., Laxon, S. W., & Ridout, A. L. (2008). Circumpolar thinning of Arctic sea ice following the 2007 record ice extent minimum. *Geophysical Research Letters*, 35(22), L22502

Green, P.J., 1995. Reversible jump Markov chain Monte Carlo computation and Bayesian model determination. *Biometrika*, *82*(4), pp.711-732.

Guerreiro, K., Fleury, S., Zakharova, E., Rémy, F. and Kouraev, A. (2016). Potential for estimation of snow depth on Arctic sea ice from CryoSat-2 and SARAL/AltiKa missions. *Remote Sensing of Environment*, 186, pp.339-349.

Guerreiro, K., Fleury, S., Zakharova, E., Kouraev, A., Rémy, F., & Maisongrande, P. (2017). Comparison of CryoSat-2 and ENVISAT radar freeboard over Arctic sea ice: toward an improved Envisat freeboard retrieval. *The Cryosphere*, *11*(5), 2059–2073. https://doi.org/10.5194/tc-11-2059-2017

Haas, C., Beckers, J., King, J., Silis, A., Stroeve, J., Wilkinson, J., Notenboom, B., Schweiger, A. and Hendricks, S. (2017). Ice and snow thickness variability and change in the high Arctic Ocean observed by in situ measurements. *Geophysical Research Letters*, *44*(20), pp.10-462.

Hallikainen, M. and Winebrenner, D.P. (1992). The physical basis for sea ice remote sensing. *Microwave remote sensing of sea ice*, 68, pp.29-46.

Hendricks, S. and Ricker, R. (2020): Product User Guide & Algorithm Specification: AWI CryoSat-2 Sea Ice Thickness (version 2.3), https://epic.awi.de/id/eprint/53331/

Jutila, Al, King, J., Paden, J., Ricker, R., Hendricks, S., Polashenski, C., Helm, V., Binder, T., Haas, C. , High-Resolution Snow Depth on Arctic Sea Ice From Low-Altitude Airborne Microwave Radar Data, in IEEE Transactions on Geoscience and Remote Sensing, doi: 10.1109/TGRS.2021.3063756., 2021a

Jutila, A., Hendricks, S., Ricker, R., von Albedyll, L., Krumpen, T., and Haas, C.: Retrieval and parametrisation of sea-ice bulk density from airborne multi-sensor measurements, The Cryosphere Discuss. [preprint], https://doi.org/10.5194/tc-2021-149, in review, 2021b.

Kern, S., & Spreen, G. (2015). Uncertainties in Antarctic sea-ice thickness retrieval from ICESat. *Annals of Glaciology*, *56*(69), 107-119.

Kern, S., & Ozsoy, B. (2019). An Attempt to Improve Snow Depth Retrieval Using Satellite Microwave Radiometry for Rough Antarctic Sea Ice. *Remote Sensing*, *11*(19), 2323. https://doi.org/10.3390/rs11192323

Kilic, L., Tonboe, R. T., Prigent, C., & Heygster, G. (2019). Estimating the snow depth, the snow–ice interface temperature, and the effective temperature of Arctic sea ice using Advanced Microwave Scanning Radiometer 2 and ice mass balance buoy data. *The Cryosphere*, *13*(4), 1283-1296.

King, J., Howell, S., Derksen, C., Rutter, N., Toose, P., Beckers, J.F., Haas, C., Kurtz, N. and Richter-Menge, J. (2015). Evaluation of Operation IceBridge quick-look snow depth estimates on sea ice. *Geophysical Research Letters*, *42*(21), pp.9302-9310.

King, J., Derksen, C., Toose, P., Langlois, A., Larsen, C., Lemmetyinen, J., ... & Sturm, M. (2018). The influence of snow microstructure on dual-frequency radar measurements in a tundra environment. *Remote Sensing of Environment*, *215*, 242-254.

Kurtz, N. T., & Farrell, S. L. (2011). Large-scale surveys of snow depth on Arctic sea ice from Operation IceBridge. *Geophysical Research Letters*, *38*(20).

Kurtz, N. T., Farrell, S. L., Studinger, M., Galin, N., Harbeck, J. P., Lindsay, R., Onana, V. D., Panzer, B., & Sonntag, J. G. (2013). Sea ice thickness, freeboard, and snow depth products from Operation IceBridge airborne data. *The Cryosphere*, 7(4), 1035–1056.

Kwok, R., Cunningham, G. F., Zwally, H. J., & Yi, D. (2007). Ice, Cloud, and land Elevation Satellite (ICESat) over Arctic sea ice: Retrieval of freeboard. *Journal of Geophysical Research: Oceans*, *112*(C12).

Kwok, R., & Cunningham, G. F. (2008). ICESat over Arctic sea ice: Estimation of snow depth and ice thickness. *Journal of Geophysical Research: Oceans*, *113*(C8).

Kwok, R., & Cunningham, G. F. (2015). Variability of Arctic sea ice thickness and volume from CryoSat-2. *Philosophical Transactions of the Royal Society A: Mathematical, Physical and Engineering Sciences*, *373*(2045), 20140157.

Kwok, R., Markus, T., Kurtz, N.T., Petty, A.A., Neumann, T.A., Farrell, S.L., Cunningham, G.F., Hancock, D.W., Ivanoff, A. and Wimert, J.T. (2019). Surface height and sea ice freeboard of the Arctic Ocean from ICESat-2: Characteristics and early results. *Journal of Geophysical Research: Oceans*, *124*(10), 6942-6959.

Kwok, R., Kacimi, S., Markus, T., Kurtz, N.T., Studinger, M., Sonntag, J.G., Manizade, S.S., Boisvert, L.N. and Harbeck, J.P., 2019. ICESat-2 Surface Height and Sea Ice Freeboard Assessed With ATM Lidar Acquisitions From Operation IceBridge. *Geophysical Research Letters*, *46*(20), pp.11228-11236.

Kwok, R., S. Kacimi, M. A. Webster, N. T. Kurtz, and A. A. Petty. "Arctic snow depth and sea ice thickness from ICESat-2 and CryoSat-2 freeboards: a first examination." *Journal of Geophysical Research: Oceans* 125, no. 3 (2020): e2019JC016008.

Landy, J. C., Tsamados, M., & Scharien, R. K. (2019). A Facet-Based Numerical Model for Simulating SAR Altimeter Echoes From Heterogeneous Sea Ice Surfaces. *IEEE Transactions on Geoscience and Remote Sensing*, *57*(7), 4164–4180. https://doi.org/10.1109/tgrs.2018.2889763

Langlois, A. and Barber, D.G. (2007). Passive microwave remote sensing of seasonal snow-covered sea ice. *Progress in Physical Geography*, 31(6), pp.539-573.

Lawrence, I. R., Tsamados, M. C., Stroeve, J. C., Armitage, T. W., & Ridout, A. L. (2018). Estimating snow depth over Arctic sea ice from calibrated dual-frequency radar freeboards. *The Cryosphere*, *12*(11), 3551-3564.

Lawrence, I.R., Armitage, T.W., Tsamados, M.C., Stroeve, J.C., Dinardo, S., Ridout, A.L., Muir, A., Tilling, R.L. and Shepherd, A. (2019). Extending the Arctic sea ice freeboard and sea level record with the Sentinel-3 radar altimeters. *Advances in Space Research*.

Laxon, S., Peacock, N., & Smith, D. (2003). High interannual variability of sea ice thickness in the Arctic region. *Nature*, *425*(6961), 947-950

Laxon, S. W., Giles, K. A., Ridout, A. L., Wingham, D. J., Willatt, R., Cullen, R., ... & Hendricks, S. (2013). CryoSat-2 estimates of Arctic sea ice thickness and volume. *Geophysical Research Letters*, *40*(4), 732-737.

Lecomte, O., 2014. *Influence of snow processes on sea ice: a model study* (Doctoral dissertation, UCL-Université Catholique de Louvain).

Maaß, N., Kaleschke, L., Tian-Kunze, X., & Drusch, M. (2013). Snow thickness retrieval over thick Arctic sea ice using SMOS satellite data. *The Cryosphere*, 7(6), 1971–1989.

Maheshwari, M., Mahesh, C., Rajkumar, K.S., Pallipad, J., Rajak, D.R., Oza, S.R., Kumar, R. and Sharma, R. (2015). Estimation of sea ice freeboard from SARAL/AltiKa data. *Marine Geodesy*, 38(sup1), pp.487-496.

Merkouriadi, I., Gallet, J. C., Graham, R. M., Liston, G. E., Polashenski, C., Rösel, A., & Gerland, S. (2017). Winter snow conditions on Arctic sea ice north of Svalbard during the Norwegian young sea ICE (N-ICE2015) expedition. *Journal of Geophysical Research: Atmospheres*, *122*(20), 10-837.

Nandan, V., Geldsetzer, T., Yackel, J., Mahmud, M., Scharien, R., Howell, S., King, J., Ricker, R. and Else, B. (2017). Effect of snow salinity on CryoSat-2 Arctic first-year sea ice freeboard measurements. *Geophysical Research Letters*, 44(20), pp.10-419.

Newman, T., Farrell, S. L., Richter-Menge, J., Connor, L. N., Kurtz, N. T., Elder, B. C., & McAdoo, D. (2014). Assessment of radar-derived snow depth over Arctic sea ice. *Journal of Geophysical Research: Oceans*, *119*(12), 8578-8602.

Ozsoy-Cicek, B., Ackley, S., Xie, H., Yi, D., & Zwally, J. (2013). Sea ice thickness retrieval algorithms based on in situ surface elevation and thickness values for application to altimetry. *Journal of Geophysical Research: Oceans*, *118*(8), 3807-3822.

Paul, S., Hendricks, S., Ricker, R., Kern, S., & Rinne, E. (2018). Empirical parametrization of Envisat freeboard retrieval of Arctic and Antarctic sea ice based on CryoSat-2: progress in the ESA Climate Change Initiative. *The Cryosphere*, *12*(7), 2437–2460. https://doi.org/10.5194/tc-12-2437-2018
Petty, A.A., Tsamados, M.C., Kurtz, N.T., Farrell, S.L., Newman, T., Harbeck, J.P., Feltham, D.L. and Richter-Menge, J.A. (2016). Characterizing Arctic sea ice topography using high-resolution IceBridge data. *The Cryosphere*, *10*(3), 1161-1179.

Petty, A. A., Webster, M., Boisvert, L., & Markus, T. (2018). The NASA Eulerian Snow on Sea Ice Model (NESOSIM) v1. 0: initial model development and analysis. *Geoscientific Model Development*, *11*(11).

Picard, G., Brucker, L., Roy, A., Dupont, F., Fily, M., Royer, A., & Harlow, C. (2013). Simulation of the microwave emission of multi-layered snowpacks using the Dense Media Radiative transfer theory: the DMRT-ML model.

Picard, G., Sandells, M., & Löwe, H. (2018). A new active/passive microwave radiative transfer model for snow (SMRT) to foster inter-comparisons of model components. In *IGARSS 2018-2018 IEEE International Geoscience and Remote Sensing Symposium*. pp. 6276-6279

Powell, D.C., Markus, T., Cavalieri, D.J., Gasiewski, A.J., Klein, M., Maslanik, J.A., Stroeve, J.C. and Sturm, M. (2006). Microwave signatures of snow on sea ice: Modeling. *IEEE Transactions on Geoscience and Remote Sensing*, 44(11), pp.3091-3102.

Pujol, M. I., Faugère, Y., Taburet, G., Dupuy, S., Pelloquin, C., Ablain, M., & Picot, N. (2016). DUACS DT2014: the new multi-mission altimeter data set reprocessed over 20 years. *Ocean Sci*, *12*(5), 1067-1090.

Quartly, G. D., Rinne, E., Passaro, M., dersen, O., Dinardo, S., Fleury, S., et al. (2019). Retrieving Sea Level and Freeboard in the Arctic: A Review of Current Radar Altimetry Methodologies and Future Perspectives. *Remote Sensing*, *11*(7), 881. https://doi.org/10.3390/rs11070881

Rae, J. G. L., Hewitt, H. T., Keen, A. B., Ridley, J. K., Edwards, J. M., & Harris, C. M. (2014). A sensitivity study of the sea ice simulation in the global coupled climate model, HadGEM3. *Ocean Modelling*, *74*, 60-76.

Remy, F., Legresy, B., & Vincent, P. (1999). New scientific opportunities from Ka-band altimetry. In *IEEE 1999 International Geoscience and Remote Sensing Symposium. IGARSS'99 (Cat. No. 99CH36293)* (Vol. 1, pp. 506-508). IEEE.

Richter-Menge, J. A., Perovich, D. K., Elder, B. C., Claffey, K., Rigor, I., & Ortmeyer, M. (2006). Ice mass-balance buoys: a tool for measuring and attributing changes in the thickness of the Arctic sea-ice cover. *Annals of Glaciology*, *44*, 205-210.

Rostosky, P., Spreen, G., Farrell, S. L., Frost, T., Heygster, G., & Melsheimer, C. (2018). Snow Depth Retrieval on Arctic Sea Ice From Passive Microwave Radiometers—Improvements and Extensions to Multiyear Ice Using Lower Frequencies. *Journal of Geophysical Research: Oceans*, *123*(10), 7120–7138. https://doi.org/10.1029/2018JC014028

Schutz, B. E., Zwally, H. J., Shuman, C. A., Hancock, D., & DiMarzio, J. P. (2005). Overview of the ICESat mission. *Geophysical Research Letters*, 32(21), L21S01.

Schröder, D., Feltham, D. L., Tsamados, M., Ridout, A., & Tilling, R. (2019). New insight from CryoSat-2 sea ice thickness for sea ice modelling. *The Cryosphere*, *13*, 125-139.

Shalina, E. V., Khvorostovsky, K., & Sandven, S. (2020). Arctic Sea Ice Thickness and Volume Transformation. In *Sea Ice in the Arctic* (pp. 167-246). Springer, Cham.

Stamnes, K., Tsay, S. C., Wiscombe, W., & Jayaweera, K. (1988). Numerically stable algorithm for discrete-ordinate-method radiative transfer in multiple scattering and emitting layered media. *Applied optics*, 27(12), 2502-2509.

Stroeve, J. C., Serreze, M. C., Fetterer, F., Arbetter, T., Meier, W., Maslanik, J., & Knowles, K. (2005). Tracking the Arctic's shrinking ice cover: Another extreme September minimum in 2004. *Geophysical Research Letters*, *32*(4).

Stroeve, J., & Notz, D. (2018). Changing state of Arctic sea ice across all seasons. *Environmental Research Letters*, *13*(10), 103001.

Stroeve, Julienne, Vishnu Nandan, Rosemary Willatt, Rasmus Tonboe, Stefan Hendricks, Robert Ricker, James Mead et al. "Surface-based Ku-and Ka-band polarimetric radar for sea ice studies." *The Cryosphere* 14, no. 12 (2020): 4405-4426.

Sturm, M., Holmgren, J. and Perovich, D.K. (2002). Winter snow cover on the sea ice of the Arctic Ocean at the Surface Heat Budget of the Arctic Ocean (SHEBA): Temporal evolution and spatial variability. *Journal of Geophysical Research: Oceans*, 107(C10), pp.SHE-23.

Sturm, M., & Massom, R. A. (2009). Snow and sea ice. *Sea ice*, *2*, 153-204.

Tilling, R. L., Ridout, A., & Shepherd, A. (2017). Estimating Arctic sea ice thickness and volume using CryoSat-2 radar altimeter data. *Advances in Space Research*. https://doi.org/10.1016/j.asr.2017.10.051

Ulaby, Fawwaz & Long, David & Blackwell, William & Elachi, Charles & Fung, Adrian & Ruf, Christopher & Sarabandi, K. & Zyl, Jakob & Zebker, Howard. (2014). Microwave Radar and Radiometric Remote Sensing.

Uotila, P., Iovino, D., Vancoppenolle, M., Lensu, M. and Rousset, C., 2017. Comparing sea ice, hydrography and circulation between NEMO3. 6 LIM3 and LIM2.

Warren, S. G., Rigor, I. G., Untersteiner, N., Radionov, V. F., Bryazgin, N. N., Aleksandrov, Y. I., & Colony, R. (1999). Snow depth on Arctic sea ice. *Journal of Climate*, *12*(6), 1814-1829.

Webster, M. A., Rigor, I. G., Nghiem, S. V., Kurtz, N. T., Farrell, S. L., Perovich, D. K., & Sturm, M. (2014). Interdecadal changes in snow depth on Arctic sea ice. *Journal of Geophysical Research: Oceans*, *119*(8), 5395-5406.

Wever, N., Rossmann, L., Maaß, N., Leonard, K. C., Kaleschke, L., Nicolaus, M., & Lehning, M. (2020). Version 1 of a sea ice module for the physics-based, detailed, multi-layer SNOWPACK model. *Geoscientific Model Development*, *13*(1), 99-119.

Willatt, R., Laxon, S., Giles, K., Cullen, R., Haas, C., & Helm, V. (2011). Ku-band radar penetration into snow cover on Arctic sea ice using airborne data. *Annals of Glaciology*, *52*(57), 197-205.

Willmes, S., Nicolaus, M., & Haas, C. (2014). The microwave emissivity variability of snow covered first-year sea ice from late winter to early summer: a model study. *The Cryosphere*, *8*(3), 891-904.

Winebrenner, D.P., Bredow, J., Fung, A.K., Drinkwater, M.R., Nghiem, S., Gow, A.J., Perovich, D.K., Grenfell, T.C., Han, H.C., Kong, J.A. and Lee, J.K., (1992). Microwave sea ice signature modeling. *Microwave remote sensing of sea ice*, 68, pp.137-175.

Wingham, D. J., Francis, C. R., Baker, S., Bouzinac, C., Brockley, D., Cullen, R., de Chateau-Thierry, P., Laxon, S. W., Mallow, U., Mavrocordatos, C., Phalippou, L., Ratier, G., Rey, L., Rostan, F., Viau, P., & Wallis, D. W. (2006). CryoSat: A mission to determine the fluctuations in Earth's land and marine ice fields. *Advances in Space Research*, 37(4), 841–871.

Wiscombe, W. J., & Warren, S. G. (1980). A model for the spectral albedo of snow. I: Pure snow. *Journal of the Atmospheric Sciences*, *37*(12), 2712-2733.

Xu, S., Zhou, L., Liu, J., Lu, H., & Wang, B. (2017). Data Synergy between Altimetry and L-Band Passive Microwave Remote Sensing for the Retrieval of Sea Ice Parameters—A Theoretical Study of Methodology. *Remote Sensing*, *9*(10), 1079.

Zhou, L., Xu, S., Liu, J., & Wang, B. (2018). On the retrieval of sea ice thickness and snow depth using concurrent laser altimetry and L-band remote sensing data. *The Cryosphere*, *12*(3), 993-1012